Stony Brook University

Theoretical study of methane activation and

methane-methanol conversion on Ni_2P model catalysts

A Thesis Presented

by

Shuaifeng Zhang

to

The Graduate School

in Partial Fulfillment of the

Requirements

for the Degree of

Master of Science

in

Chemistry

Stony Brook University

May 2017

Stony Brook University

The Graduate School

Shuaifeng Zhang

We, the thesis committee for the above candidate for the

Master of Science degree, hereby recommend

acceptance of this thesis.

Ping Liu, Ph.D., Advisor
Chemist, Brookhaven National Laboratory

Jin Wang, Ph.D., Chair
Professor, Department of Chemistry and physics

Carlos Simmerling, Ph.D., Third Member
Professor, Department of Chemistry

This thesis is accepted by the Graduate School

Charles Taber
Dean of the Graduate School

Abstract of the Thesis

Theoretical study of methane activation and

methane-methanol conversion on Ni_2P model catalysts

by

Shuaifeng Zhang

Master of Science

in

Chemistry

Stony Brook University

2017

Methane (CH_4) is the principle component of natural gas, and a controlled methane conversion pathway may influence chemical industry significantly. Nickel catalyst is a one of promising catalysts for methane activation, but suffering severe carbon deposition and degradation under reaction conditions. In this study, of the activation of CH_4 in presence of water on nickel phosphide, $Ni_2P(0001)$, model surfaces were investigated, where the surface terminated by both Ni_3P_2 and Ni_3P_2+P were taken into considerations. Density functional theory (DFT) calculations were performed to determine structures and energetics of intermediates and transition states along the reaction pathways during CH_4 activations. Compared to pure Ni, Ni_2P promotes the water dissociation over CH_4 dissociation significantly, which results in the formation of Nickel hydroxyphides or oxyphosphides. Among the systems studied, oxygen adsorbed at the Ni-P bridge site of Ni_3P_2-terminated $Ni_2P(0001)$ surface displays the highest activity toward C-H bond breaking and direct formation of methanol. Our results indicate that the formation of phosphides hinders the CO formation on pure Ni, while it opens a new route toward direct methane activation to methanol, an economical way to obtain valuable chemicals directly from abundant natural gas resources. It also hinders the surface poisoning, which is a big challenge for Ni catalysts. The unique catalytic behavior of Ni_2P during methane reforming is associated with the synergy between Ni and P sites.

To Ywwuyi.

Human praise is the praise of courage!

We will never forget 2015 summer.

May Chiyoda watch over you.

Table of Contents

List of Figures

List of Tables

List of Abbreviations

DFT	density functional theory
DOS	density of state
GGA	generalized gradient approximation
NEB	nudged elastic band
PAW	projector augmented-wave
PDOS	projected density of state
PW91	Perdew-Wang approximation
TS	transition state
TST	transition state theory
VASP	Vienna Ab initio Simulation Package
VTST	VASP transition state theory
ZPE	zero-point energy

Acknowledgments

I want to thank Dr. Ping Liu for giving me the great opportunity to do my research in Brookhaven Nation Laboratory, with the cluster there I could finish this calculation research. Without her guidance and advice, I could not finish this project, and I appreciate her serious research attitude and benevolent personality.

It was a great experience to do my research in BNL, here I met many helpful friends. I would like to thank Shizhong Liu, Haoyue Guo, Zhiwen Zhou, Dr. Shyam Kattel, Dr. Zhijun Zuo and Dr. Zhao Jiang for their help in academic field. When my research or analysis got stuck, their advice always gave me inspiration to overcome the trouble. From them I did learn a lot.

Also, I am grateful to other group members, Dr. Jose Rodriguez, Dr. Sanjaya Senanayake etc. Although I did not have chance to work on the same project with them, it was a pleasure to be in such a good group and have their company.

I would also like to thank staff members in Center for Functional Nanomaterials (CFN) and Scientific Data & Computing Center (SDCC) who maintain the cluster running. I did not meet them at all, but without the cluster, this study would not be able to start in the beginning.

Special thanks should be given to my committee members, Professor Jin Wang and Professor Carlos Simmerling for their support during M.S. defense.

Without my family's support, I could not be here. Thank them for everything they did.

Finally, I want to thank you, whoever reading this piece of work, for whatever reason. Wish you a good day. If you can get any useful information, impressive idea or even just good feeling from this thesis, that is all I want.

1. Introduction

1.1 Methane Activation

The utilization of methane (CH_4) has attracted more and more attentions to produce fine commodity chemicals, due to the enormous reserves and resources on earth. CH_4 is the principle component (70% - 90% by volume) of natural gas, a main by-product of petrochemical plants, which constitutes one of the most abundant carbon resources of the world [1-2]. In addition, it is also part of the renewable biogas formed by anaerobic digestion of energy crops, residues and wastes (50 % - 70 % by volume). However, due to the inert chemical property[3], the conversion of CH_4 is neither efficient nor well-controlled. Currently 90% of CH_4 is burned to create energy ($CH_4 + 2O_2 \rightarrow CO_2 + 2H_2O$), which emits carbon dioxide (CO_2), one of greenhouse gases. In addition, there are only small number of industrial conversion pathways for CH_4 to synthesis gas via oxidation or reforming, or chemicals including methanol (CH_3OH) via oxidation, chloromethane via chlorination, acetylene via partial combustion or electro pyrolysis, and hydrogen cyanide via reaction with ammonia[1].

The conversion of CH_4 to syngas is the main technology for CH_4 conversion and applied in industry [4-6]. Syngas is a fuel gas mixture of carbon monoxide (CO) and hydrogen (H_2), and usually contains a small amount of CO_2. The method of converting CH_4 into synthesis gas was found in 1902 by Sabatier and Senderens[7-8]. Currently, depending on the H_2/CO ratio of product, the CH_4 conversions are divided into three ways: (1) dry reforming of CH_4 ($CO_2 + CH_4 \rightarrow 2CO + 2H_2$) [9-11], one of the effective ways for utilizing two of the greenhouse gases. It produces H_2 and CO with the ration of 1, which is desirable for long chain hydro-carbons produced by Fischer–Tropsch synthesis [12-14]; (2) steam reforming of CH_4 ($CH_4 + H_2O \rightarrow CO + 3H_2$). It allows the high selective production of H_2 over CO with the ration of 3, which can be used to hydroformylation reactions or produce pure hydrogen by removing CO for ammonia synthesis or hydrogenation reactions; (3) partial oxidation of CH_4 ($CH_4 + ½O_2 \rightarrow CO + 2H_2$) [15]. It is a promising but not yet industrially applied method for converting CH_4 to synthesis gas with a ratio of nearly 2:1, which is suitable for CH_3OH production [16].Compared with natural gas, syngas has even lower energy density, but can be used as resource for production of ammonia, CH_3OH and synthetic hydrocarbon fuels. However, the conversion of CH_4 into syngas is often energy intensive and represents the major expense in chemical production. In addition, carbon

monoxide is toxic, the application of syngas in daily life may be a security risk. Therefore, syngas is not an ideal product compared with CH_4 derivatives such as CH_3OH.

My research is focused on the direct conversion of CH_4 to CH_3OH ($H_2O + CH_4 \rightarrow CH_3OH + H_2$) at low temperatures. There is significant interest in developing a direct method of converting CH_4 to CH_3OH as it can eliminate the need for expensive steam reforming and is more economical. CH_4- CH_3OH direct oxidation has been studied for decades, types of catalysts and systems investigated [17-20]; however, it is currently still not industrialized, which suffers from low CH_4 conversions by approximately 1% and requires harsh reaction conditions to break strong C−H bonds [21]. In addition, the selectivity to CH_3OH is also low due to that CH_3OH is more reactive than CH_4, which can result in oxidations into formic acid or carbon oxides under reaction conditions [22]. Thus, the growing need for development of inexpensive catalysts, being able to facilitate the CH_4 conversion and promote selectively to CH_3OH production for CH_4 conversion to CH_3OH, has sparked considerable interests.

1.2 Catalyst for Direct Methane Activation to Methanol

Direct conversion of CH_4 to CH_3OH requires to trap the CH_3OH as a product or intermediate. Therefore, it is essential to find a catalyst that can activate CH_4 in an efficient way at low temperatures (< 500 K) [23-24]. This is difficult because the C-H bond in CH_4 has the highest bond energy (104 kcal/mol) amongst organic compounds and breaking the first C-H bond of CH_4 has been proposed as the most difficult step for the conversion on various metal and metal alloy catalysts [21, 25-28]. As a result, the reaction temperature has to raise. Nature provides the perfect catalyst, the enzyme methane monooxygenase. The enzyme enables the temperature lowered down to room temperature for the CH_4- CH_3OH conversion, and the reaction is probably carried out by a group of di-iron or di-/tri-copper active clusters [29-30]; however, it cannot be used for industrial-scale reactions [30-31]. These enzymatic structures provide intriguing structural motifs for the development of biomimetic catalytic systems toward the activation of CH_4.

Extensive studies have been performed to study the bio-inspired catalysts. It has been found that iron- or copper-exchange zeolites can mimic the nuclearity and reactivity of active sites of the CH_4 monooxygenase.[24, 32-35] In the structure of the zeolites, CH_3OH can be produced by

sequential dosing of O_2 and CH_4, and then flushed out with water. A direct catalytic transformation of CH_4 to CH_3OH is also possible. Theoretical studies showed that the oxygen sites directly interacted with Cu or Fe ions are active, being able to break the C-H bond with lower barrier than on metal sites via either Langmuir-Hinshelwood (LH) mechanism [33] or Eley-Rideal (ER) mechanism [35]; yet the first C-H bond breaking of CH_4 still seems to be the most difficult step. Recently, our group at Brookhaven discovered an inverse $CeO_2/Cu_2O/Cu(111)$ model catalyst, being able to activate CH_4 at room temperature and produce *C, *CH_x fragments and *CO_x species on the oxide surface[36]. The addition of water to the system leads to a drastic change in the selectivity of CH_4 activation yielding only adsorbed *CH_x fragments. At a temperature of 450 K, in the presence of water, a CH_4 to CH_3OH catalytic transformation occurs with a high selectivity. DFT calculations demonstrate that *OH groups bound with the interfacial Ce sites formed by the dissociation of water saturate the catalyst surface, removing sites that could decompose *CH_x fragments, and generating centers on which CH_4 can directly interact to yield CH_3OH. By comparison, *OH groups interacted with Cu sites on the Cu_2O film, where the direct CH_4 dissociation on *OH is highly activated.

1.3 Motivation for the Study of Ni_2P

Nickel is one of common catalysts with low cost that applies for CH_4 activation reactions. Due to severe carbon deposit problem, nickel catalyst for CH_4 conversion was not commercialized.[11, 37-41] According to Lercher et al., the formation of carbon deposit on Ni surface is because that the carbon oxidation rate is much lower than carbon formation rate.[42] Abild-Pedersen et al. conducted a theoretical study, and listed three different types of graphene growth mechanisms, which agreed with that the accumulation of carbon would form carbon deposit obstructing further reaction.[43] Reduction of carbon deposit is the key factor of Ni-based catalysts. To release the carbon deposition, extensive efforts have been made including raising the temperatures above 1000 K and excessing CO_2 to facilitate the reverse Boudouard reactions, decreasing the particles or deactivating Ni sites with hydrogen, oxygen or sulfur [42, 44-46].

My research interest aims to investigate the effect of Phosphorus (P) on the CH_4 activation activity of Ni, specifically direct CH_4 to CH_3OH conversion on the formation of nickel phosphide (Ni_2P). Ni_2P has been investigated in many catalytic activities. The high activity and

thermostability make it a competitive candidate as hydrodesulfurization (HDS) catalyst, and also for hydrodenitrogenation reaction.[47-49] Ni_2P can also serve as catalysts for hydrogen evolution reactions (HER)[50-51] and water gas shift (WGS) reaction[52]. The mechanistic studies based on theoretical calculations show that the presence of P modifies the activity of Ni sites via both electronic and ensemble effects. In term of electronic effect, the formation of phosphides leads to partial oxidation of Ni, which weakens the Ni-adsorbate interaction and therefore surface poisoning. In addition, the P sites participate in the reaction directly via the ensemble effect: it not only decreases the number of active Ni sites and therefore the coverage of surface poisoning, but also participates in the reaction directly by providing the moderate binding to the reaction intermediates by itself or via the synergy with Ni sites to release the surface poisoning and therefore promote the overall conversion [49-50, 52].

Now the question is whether such P-induced poisoning-release can also help to hinder the carbon deposition and enhance the CH_4 activations. In contrast to the efforts understanding the effect on O, S, and H on Ni during the CH_4 activation reactions, little has been reported so far for P. In this study, we will carry out DFT calculations in combination with the kinetic Monte Carlo (KMC) simulations investigate the CH_4 dissociation and reforming on the model Ni_2P (0001) surfaces. Our goal is to demonstrate the effect of P on the binding property of Ni_2P, establish the reaction network and identify the active sites during CH_4 activation reactions.

2. Theoretical method

2.1 Density Functional Theory

Density functional theory (DFT) is one of *ab initio* methods, which means from the beginning, in other words, only Schrödinger equation and basic physical constants, for instance, Planck constant and mass of electron, are used for calculation. In Schrödinger equation (Eq. 1), the Hamiltonian ($\hat{H}$) of a system consists of kinetic energy and potential energy in a many-body system.

$$\hat{H} = \hat{T} + \hat{V} \quad (1)$$

Here $\hat{T}$ and $\hat{V}$ correspond operator of kinetic energy and potential energy respectively. And these operators contain contribution from nucleus and electrons.

$$\hat{T} = \hat{T}_N + \hat{T}_e = -\sum_I \frac{\hbar^2}{2M_I} {\nabla_I}^2 - \sum_i \frac{\hbar^2}{2m_i} {\nabla_i}^2 \quad (2)$$

$$\hat{V} = \hat{V}_{NN} + \hat{V}_{Ne} + \hat{V}_{ee} = \sum_I \sum_{J<I} \frac{Z_I Z_J e^2}{r_{IJ}} - \sum_I \sum_j \frac{Z_I e^2}{r_{Ij}} + \sum_i \sum_{j<i} \frac{e^2}{r_{ij}} \quad (3)$$

Here a system containing *I* nucleus and *i* electrons is considered. $\hat{T}_N$, $\hat{T}_e$, $\hat{V}_{NN}$, $\hat{V}_{Ne}$ and $\hat{V}_{ee}$ represent kinetic energy of nuclei, kinetic energy of electrons, potential energy between nuclei, potential energy between nucleus and electron and potential energy between electrons. ħ, M_I, m_i, Z, e, r, represent Planck constant, mass of nucleus, mass of electron, charge coefficient, charge of electron and distance, respectively. And ${\nabla_I}^2$ and ${\nabla_i}^2$ are Laplacian for nucleus and electron. As shown above, kinetic and potential energy depend on momentum, mass, position and charge of particles. If we do the calculation with exactly Schrödinger equation, a huge amount of computations will be required, that is both uneconomical and time-consuming.

Therefore, some approximation is necessary to simplify the calculation. The basic idea of DFT is considering many electrons as an electron gas. With this transformation, the variables for all electrons can simplify to three spatial coordinates and the electron density at that point. This simplification is put forward as Thomas-Fermi model[53], and was proved theoretically by Hohenberg-Kohn theorems[54]. According to Hohenberg and Kohn, the ground-state potential of a many-body system is a functional only of the electron density.[55] In Kohn-Sham formalism, the Schödinger equation is given as

$$\left(-\nabla^2 + V_H[\rho(\vec{r})] + V_N(\vec{r}) + V_{XC}[\rho(\vec{r})]\right)\psi_i(\vec{r}) = E_i\psi_i(\vec{r}) \quad (4)$$

where ∇^2 is the kinetic energy of the electrons; V_H is the Hartree term, accounting for the electron-electron repulsion (an effective potential representing the average effect of the repulsive interactions of all other electrons); V_N is the nuclei potential; V_{XC} represents the exchange-correlation energy, including Pauli exclusion and spin effect. The exact form of V_{XC} cannot be obtained, so there are different approximations.

The DFT calculation of this study was performed using Vienna Ab initio Simulation Package (VASP). VASP is a program for atomic scale chemical modelling, and can computes approximate solution to Schrödinger equation of many-body system with DFT method.[56] The calculation was run on Center for Functional Nanomaterials institutional cluster, supported by the Scientific Data Computing Center at Brookhaven National Laboratory.

DFT calculation was performed with periodic boundary conditions to optimize the structures of surfaces with and without adsorbates as well as calculate binding energy and the reaction energy, the energy cost or release from one state, a reactant, to the next, a product. The exchange-correlation energy was calculated with generalized gradient approximation (GGA) using the method of Perdew-Wang (PW91)[57]. The projector augmented-wave (PAW) method was used to describe electron-ion interaction.[58] The calculation was performed with cut-off energy of 520eV. The structure of Ni_2P bulk is optimized base on the former study[59-60] and the optimization was performed with and k-point Gamma grids of 4×4×8, all atoms and lattice constants relaxed. With the optimized bulk, (0001) surfaces of Ni_2P with different terminations were also considered using a six-layer slab with a $\sqrt{3} \times \sqrt{3}$ array in each layer and a 15 Å vacuum to separate the two supercells along the surface direction. The top two layers were allowed to relax with the adsorbate, and the bottom 4 layers were fixed at the optimized bulk position. These optimizations were performed with supercell constant fixed and Brillouin zone was sampled with the k-point Monkhorst-Pack[61] grid of 5×5×1.

2.2 Transition State Search

For a reaction going from a reactant to a product, the corresponding thermodynamics, or the reaction energy can be obtained using the ground-state DFT calculation as indicated in Section 2.1. However, to gain better understanding of the reaction, the transition state search is a step necessary to estimate the reaction rate, which can be measured experimentally. According to transition state theory (TST), TS is a state between a reactant and a product with higher energy,

and the energy difference between the reactant and TS corresponds to activation barrier, an energy which is required to overcome to allow the conversion of the reactant to the product. But since the transition state is not stable, it cannot be obtained with structure optimization using standard DFT.

An important problem of TS study is finding out the lowest energy path for reaction. To obtain final state, the reaction may go through different paths, but from the view of energy, the reaction should go through the lowest energy path. As we can expect, the energy barrier should be a saddle point of high dimensional space. Many methods were developed to find out the saddle point.[62] A traditional thought starts at initial state and trace a path of slowest ascent[63-64], but this pathway may not lead to the saddle point. One method is to calculate the normal modes of a local harmonic approximation of the potential energy surface and then follow the modes until a saddle point is found.[65-66] Other methods use the two point boundary condition of initial and final configuration to get the saddle point. This type of methods optimizes several intermediate along reaction path, and each image finds the lowest energy with equal spacing to neighbor maintained. Nudged elastic band (NEB) method is one of these methods. The optimization is constrained by adding spring forces along the band between images and projecting out the component of the force perpendicular to the band[67].

NEB was employed for this study, and the calculation was also performed with VASP. Because of the limitation of VASP NEB features, the VASP transition state theory (VTST) tools was compiled to original VASP to obtain a better performance. The initial and final states were chosen among optimized adsorbents or co-adsorbents geometry, with comprehensive consideration of geometry stability and movement distance. The calculation was performed with the same manner as optimization, and along the path, 4 intermediates images were employed to describe the reaction.

3. Result and Discussion

3.1 Structure of Ni_2P

3.1.1 Ni_2P bulk

Ni_2P has a hexagonal structure with space group $P_{\bar{6}2m}$, as a lattice shown in Fig. 1(a). Ni_2P consists of two types of layers, Ni_3P_2 (Fig. 1(b)) and Ni_3P (Fig. 1(c)), arranged alternately along the (0001) direction to give the full stoichiometry of the bulk.

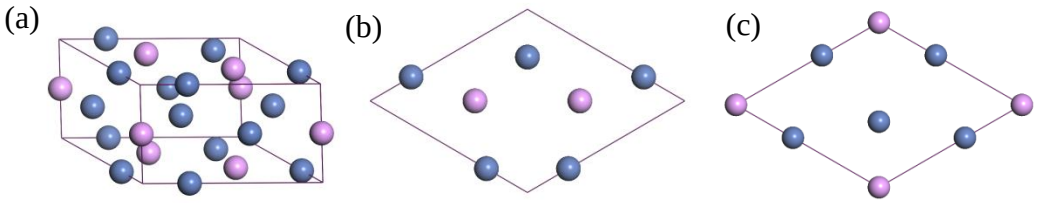

Fig. 1 Structure of Ni_2P bulk (a), Ni_3P_2- layer (b)Ni_3P-layer (c)Ni_3P_2-layer (Purple: P; Blue: Ni).

The bulk optimization gave the lattice constants of a = 5.87 Å and c = 3.36 Å, which agrees well with previous first-principles study[52, 68] and experiments[47, 59-60] results. The nearest distance of Ni-Ni and Ni-P bond on Ni_3P_2 plane is 2.65 Å and 2.20 Å respectively, and the nearest distance of Ni on Ni_3P_2 plane and P on Ni_3P plane is 2.27 Å, in agreement with the study by Li et al.[68]. The consistency between the present calculations and the previous studies in both theory and experiment assures that the parameter setups in VASP are appropriate to describe Ni_2P.

3.1.2 Ni_2P surface

The (0001) surface of Ni_2P is the most stable orientation and has been mostly studied. According to theoretical studies by our group and other groups, the Ni_3P_2 (Fig. 2(a)) is preferred termination of the Ni_2P(0001) surface[49, 68]. This is opposite to scanning tunneling microscopy (STM) results by Moula et al. where the P atoms of Ni_3P are observed on surface.[69] Recently, Yuan et al. and Wexler et al. demonstrated that the Ni_3P_2+P-terminated Ni_2P(0001) surface was more stable than the Ni_3P_2-terminated based on DFT calculation[70-71]. As shown in Fig. 2(b), Ni_3P_2+P-terminated Ni_2P(0001) surface corresponds to the configuration, where the Ni sites of Ni_3P_2-terminated Ni_2P(0001) surface are covered by P adatoms. Such morphology perfectly agrees with the STM measurement. However, Ni_3P_2+P termination requires phosphorus-enriched condition. In addition, the real termination may not be a single stoichiometry, but a mixture of

different types of stoichiometry. Besides (0001) termination, few planes were investigated with calculation method mainly because its geometric complexity. Yuan et al. studied the $Ni_2P(10\bar{1}0)$ surface annealed at 723K, and found the reconstructed structure is similar to the (0001) plane.[71]

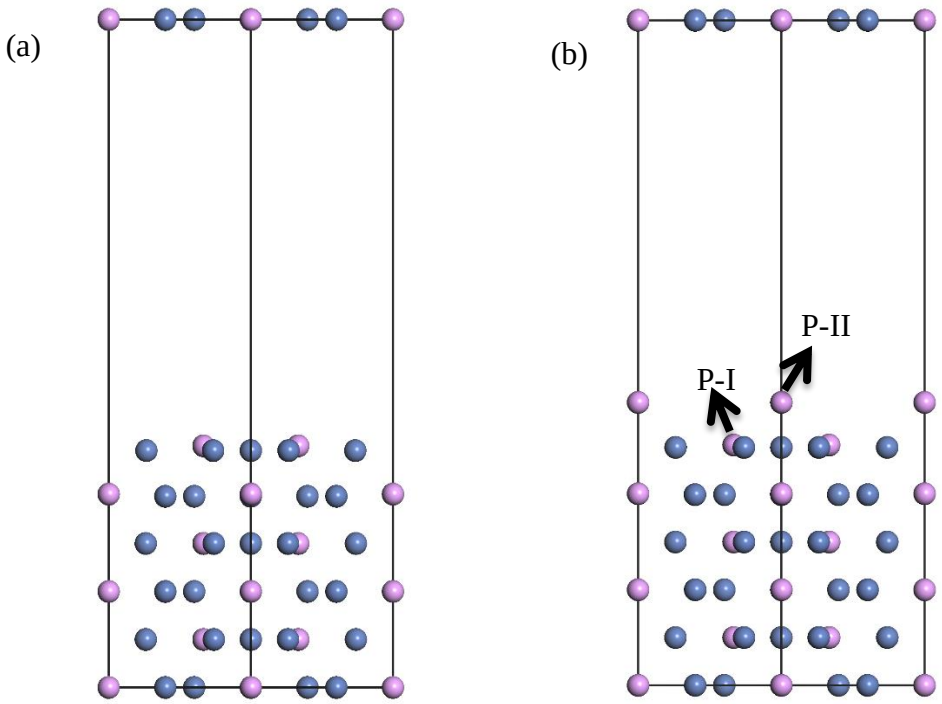

Fig. 2 Side view of supercell Ni_2P (0001) with (a) Ni_3P_2 termination and (b) Ni_3P_2+P termination (Purple: P; Blue: Ni).

In this study, $Ni_2P(0001)$ surface with both Ni_3P_2 and Ni_3P_2+P terminations were investigated for CH_4 activation using the supercell as shown in Fig. 2. Enough vacuum space was reserved for further investigated. After the optimization, small displacement from the bulk position was observed after relaxation (Table 1). On Ni_3P_2 terminated $Ni_2P(0001)$, the P atoms move outward the surface, while Ni atoms move inward, in agreement with Li's result[68]. With the additional P covered on the surface, the displacement of Ni atoms is decreased on Ni_3P_2+P-terminated surface, though the direction is kept the same. And the extra P atom above Ni site moved inward, that suggests there is strong interaction between the extra P adatom and Ni_3 site. The distance between Ni and extra-P atom is 2.20 Å, in consistent with the Wexler's result [70].

Table 1 Bond length (Å) of Ni_2P bulk and $Ni_2P(0001)$ with both Ni_3P_2 and Ni_3P_2+P terminations and displacement (Å) of each atom on the surface after termination optimization.

	Displacement			**Bond length**		
	Ni	P	P (extra)	Ni-Ni	Ni-P	Ni-P(extra)
Bulk	0	0	0	2.65	2.20	2.27
Ni_3P_2	0.12	0.07	-	2.70	2.19	-
Ni_3P_2+P	0.03	0.06	0.13	2.66	2.20	2.20

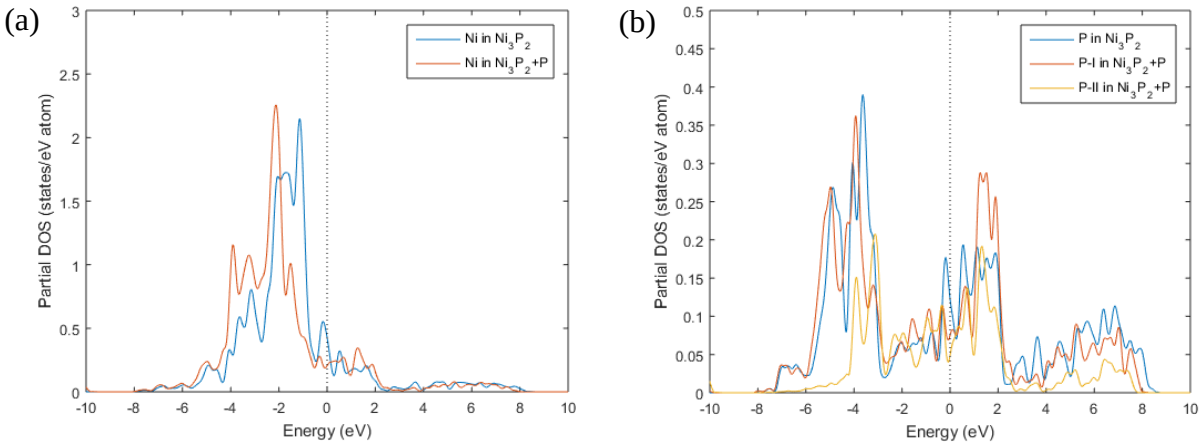

Fig. 3 Projected density of states (PDOS) of (a) Ni 3d and (b) P 3p on $Ni_2P(0001)$ with both Ni_3P_2 (blue lines) and Ni_3P_2+P (orange lines) terminations, where the solid and dashed orange lines represent two different types of P atoms, P-I and P-II, on Ni_3P_2+P-terminated $Ni_2P(0001)$, respectively.

The calculated projected density of states (PDOS) of Ni and P atoms on the surface (Fig. 3) agrees well with the previous study by Li et al.[68]. Compared with Ni_3P_2 termination, with the influence of extra P atom, the PDOS peaks shape changes slightly. With the extra P covered the Ni sites of Ni_3P_2-terminated $Ni_2P(0001)$, the Ni 3d states are shifted away from Fermi level. It suggests that the Ni sites are further oxidized by the presence of extra P (Fig. 3a). In term of P sites (Fig. 2b), there are two different types of P sites on the surface of Ni_3P_2+P-terminated $Ni_2P(0001)$. Type I, P-I, corresponds to the P sites on Ni_3P_2-terminated $Ni_2P(0001)$, and type II, P-II, represents the extra P adsorbed on Ni_3P_2-terminated $Ni_2P(0001)$. There is a slightly increase in DOS for the occupied states of P-I on the surface (Fig. 3b). That is, the introduction of extra P-II on the surface weakens the Ni-P-I interaction on the Ni_3P_2-terminated $Ni_2P(0001)$ surface due to the strong Ni-P-II interaction, which leads to a more oxidized P states than that of P-I.

According to the results on PDOS, the adsorption of extra P is likely to decrease the binding property of Ni_3P_2-terminated $Ni_2P(0001)$ due to both electronic and ensemble effects. In term of electronic effect, it leads to the further oxidation of Ni sites on the surface and decreases the ability to donate electrons for stabilizing the reaction intermediates. Regarding ensemble effect, the extra P partially blocks the active Ni sites, which hinders the direct interaction of the reaction intermediates with Ni.

3.2 Binding Property of Ni_2P Surface

To evaluate the proposed binding properties according to the calculated PDOS, in this section, we optimized the binding geometry and calculated the binding energy of reaction intermediates involved in CH_4 activation on optimized Ni_3P_2-terminated and Ni_3P_2+P-terminated $Ni_2P(0001)$ surfaces as shown in section 3.1. Different adsorption sites were considered on each surface (Fig. 4), where the most stable adsorption site for each adsorbent was used to describe the reactions related.

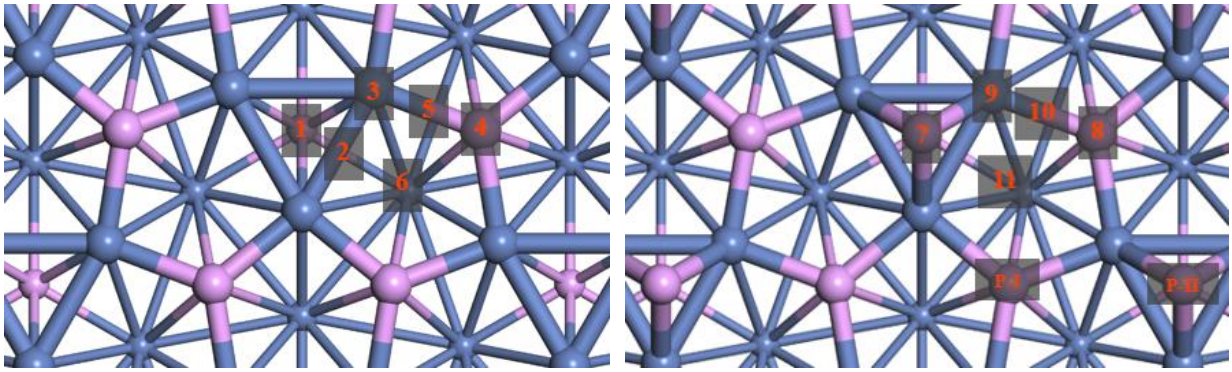

(a) (b)

Fig. 4 Top view (a) Ni_3P_2-terminated and (b) Ni_3P_2+P-terminated $Ni_2P(0001)$ surface (Blue: Ni; Purple: P).

Because of the symmetry of geometries of terminations, in both supercells, a three-fold rotation axis and a mirror plane exist. Therefore 6 adsorption sites on Ni_3P_2-terminated and 5 adsorption sites on Ni_3P_2+P-terminated surface were considered. On the Ni_3P_2 surface layer (Fig. 4a), the adsorption sites include Ni_3 3-fold hollow (site 1), Ni_2 bridge (site 2), Ni_1 atop (site 3), P atop (site 4), Ni-P hybrid bridge (site 5) and Ni_3-P_2 hybrid 5-fold hollow (site 6). While on the Ni_3P_2+P surface layer (Fig. 4b), because of the extra P atom occupying the Ni_3 site, new sites are

formed, including P-II atop (site 7), P-I atop which shared Ni with P-II (site 8), Ni-P-II bridge (site 9), Ni-P-I bridge (site 10) and Ni_3-P_2 5-fold hollow (site 11).

The considered adsorbates in the present study included the potential intermediates and products involved in CH_4 dissociation, water (H_2O) dissociation, and oxidation of dissociated fragments form CH_4. The adsorption energy was calculated as

$$E_X = E(X^*) - \mathrm{E}(surf) - E(X) \quad (5)$$

Here $E(X^*)$ is the total energy of the adsorbed species, X, on the surface, where "*" represents for a surface site. $E(surf)$ corresponds to the total energy of bare surfaces. $\mathrm{E}(X)$ stands for the energy X in gas phase. In the present calculation, $\mathrm{E}(X)$ was expressed with respect to $\mathrm{E}(CH_4)$, $\mathrm{E}(H_2)$, $\mathrm{E}(H_2O)$, $\mathrm{E}(CO_2)$, $\mathrm{E}(CO)$, or $\mathrm{E}(CH_3OH)$. The adsorption energies on Ni_3P_2-terminated and Ni_3P_2+P-terminated $Ni_2P(0001)$ surfaces were listed in Table 2 and Table 3, respectively.

Table 2 Adsorption energies (eV) on Ni_3P_2-terminated $Ni_2P(0001)$ surface*

	1	**2**	**3**	**4**	**5**	**6**
E_{*H}	**-0.59(-0.44)**	→1	→1	+0.11	-0.01	→1
E_{*CH_3}	**+0.48(+0.14)**	→1	+0.64	+0.57	+0.75	→3
E_{*CH_2}	+1.18(+0.57)	→1	→1	→5	**+1.12(+0.56)**	→5
E_{*CH}	**+1.50(+0.63)**	→1	→1	+3.36	+2.69	+2.55
E_{*C}	**+2.86(+1.73)**	→1	→1	+3.19	+4.83	+3.28
E_{*OH}	**-0.35 (-0.59)**	→1	→1	+0.12	+0.21	→1
E_{*O}	+0.39 (-0.16)	→1	→1	→5	**+0.38 (-0.16)**	→5
E_{*H_2O}	→3	→3	**-0.36**	-0.03	→3	-0.11
E_{*CO}	**-1.88 (-1.85)**	→1	→1	-0.14	→1	→1
E_{*CO_2}	+0.13	+0.14	-0.08	-0.05	**-0.09**	-0.08
E_{*CH_4}	**-0.11**	**-0.11**	-0.10	-0.10	**-0.11**	**-0.11**
E_{*CH_3OH}	-0.01	-0.11	**-0.17**	+0.09	→3	→3

* The most stable adsorption is highlighted in bold. The values in parenthesis are zero-point energy (ZPE) corrected adsorption energies, which will be used for the following study.

Most adsorbents prefer the Ni sites on Ni_3P_2-terminated $Ni_2P(0001)$ surface. The Ni_3 sites (Site 1, Fig.4a) is the most stable sites for adsorption of hydrogen (*H), methyl (*CH_3), methylene (*CH_2), methylidyne (*CH), hydroxyl (*OH), carbon monoxide (*CO) and carbon (*C), and the Ni_1 top sites (Site 3) adsorb H_2O and CH_3OH the most strongly (Table 2). Both P sites (Site 4) and Ni-P hybrid sites (Site 5 and Site 6) can also participate in the binding directly, though these sites either cannot stabilize the adsorbate or bind the species less strongly than the

Ni sites (Table 2). For methylene (*CH_2) and oxygen (*O), Ni-P bridge site (Site 5) provides almost the same adsorption energy as the Ni_2 site (Site 1). *CO shows the strongest site preferential, where the Ni_3 site is significantly more preferred than the other sites and can result in the CO poisoning; in contrast, *CH_4 displays the least preference, which binds weakly on all sites. CH_4, CO_2 and CH_3OH all interact weakly with the surface. The site preference from current calculations for *H_2O, *OH, *CO and *H agree with the previous study by Liu et al.[52].

Table 3 Adsorption energies (eV) on Ni_3P_2+P-terminated $Ni_2P(0001)$ surface

	7	**8**	**9**	**10**	**11**
E_{*H}	**-0.23(-0.03)**	+0.33	-0.01	+0.25	+0.33
E_{*CH_3}	**+0.13(-0.13)**	+0.74	→7	→8	→8
E_{*CH_2}	+1.44	→10	**+1.13(+0.56)**	+1.53	→9
E_{*CH}	+3.08	→10	+2.33	**+1.97(+1.13)**	+2.09
E_{*C}	+5.28	→10	**+2.97(+1.84)**	+3.45	+3.91
E_{*OH}	**-0.27(-0.53)**	+1.56	→7	+0.88	→7
E_{*O}	**-0.25(-0.80)**	→10	→7	+0.94	→10
E_{*H_2O}	-0.04	-0.07	-0.05	→8	→8
E_{*CO}	-0.12	+0.36	**-0.68(-0.61)**	0.00	→9
E_{*CO_2}	**+0.02**	**+0.02**	+0.64	+0.06	+0.96
E_{*CH_4}	-0.02	**-0.03**	→11	-0.02	**-0.03**
E_{*CH_3OH}	+0.18	+0.15	**+0.02**	→9	→9

* The most stable adsorption is highlighted in bold. The values in parenthesis are zero-point energy (ZPE) corrected adsorption energies, which will be used for the following study.

On Ni_3P_2+P-terminated $Ni_2P(0001)$ surface, the introduction of extra P (P-II, Fig. 4b) blocks the active Ni_3 sites. The top of P-II (Site 7) becomes the preferential adsorption site for *H, *CH_3, *OH, and *O. In addition, Ni-P bridge sites also help. The Ni-P-II bridge (Site 9) interacts well with *CH_2, *C, and *CO, where the adsorption results in the displacement of P-II from Ni_3 hollow site, while the Ni-P-I bridge (Site 10) stabilizes *CH. Upon going from Ni_3P_2-terminated to Ni_3P_2+P-terminated $Ni_2P(0001)$ surface, the interactions of the weakly bound molecules, like CH_4, CO_2 and CH_3OH, with the surface are further weakened, though the variation is rather small (< 0.2 eV). Subtle weakening in binding energy is also observed for *CH_2, *OH and *C. By comparison, the weakening effect on H_2O is more significant, where the molecule is not adsorbed with the presence of P-II; besides, *H, *CH and *CO are also destabilized greatly, where the destabilization of *CO is the most significant with the binding

energy decreased by more than 1 eV. That is, the introduction of P-II on $Ni_2P(0001)$ likely results in deactivation of the surface, which particularly enables the release of the possible CO poisoning on the surface. The exception is observed for $*CH_3$ and *O. The P-II sites are more active than the Ni_3 sites for adsorption, together with the formation of methylenephosphine ($*PCH_3$) and P oxides (*PO) species, respectively.

Overall, the electronic effect on Ni_3P_2-terminated $Ni_2P(0001)$ is very small. The Ni_3 sites provides the similar binding strength as that on Ni(111). For instance, the CO binding on Ni_3P_2-terminated $Ni_2P(0001)$ (-1.88 eV) and Ni(111) (-1.83 eV) [72] is about the same. However the ensemble effect indeed decreases the number of active Ni_3 sites and makes the Ni_3 sites more flexible for accommodating the adsorbates compared to Ni(111). With the introduction of extra P, the ensemble effect is enhanced on Ni_3P_2+P-terminated $Ni_2P(0001)$, where a further bond-weakening is observed. Now the question is whether such decrease in bonding will be able to help in releasing the carbon deposition on Ni catalysts under CH_4 activation conditions. To answer that, we will take a further step in Section 3.3to investigate the activity of Ni_2P with both Ni_3P_2 and Ni_3P_2+P terminations towards CH_4 dissociation, H_2O dissociation and CH_4 reforming reactions based on the DFT results on the adsorptions of reaction intermediates.

3.3 Activity of Ni_2P Surface

3.3.1 Methane Dissociation

CH_4 dissociation contains sequential steps of dehydrogenation and the production of carbon: $* CH_4 \rightarrow * CH_3 + * H$, $* CH_3 \rightarrow * CH_2 + * H$, $* CH_2 \rightarrow * CH + * H$, $* CH \rightarrow * C + * H$, [27, 72-73] A potential energy diagram for CH_4 dissociation on Ni_3P_2-terminated and Ni_3P_2+P-terminated $Ni_2P(0001)$ surfaces is shown as Fig. 5. The reaction on both surfaces is highly endothermic. That is, C-H bond cleavage on $Ni_2P(0001)$ surfaces is thermodynamically unfavorable. The Ni_3P_2-terminated surface behaves similarly as Ni(111), [72] where a significant energy increase (> 1 eV) is observed for *CH → *C, suggesting that *CH is the most stable intermediate for CH_4 dissociation. However, this is not the case for Ni_3P_2+P-terminated surface, where the energy keeps rising after the first C-H bond cleavage and the formation of $*CH_3$. It is likely that the introduction of extra P is able to vary the selectivity of $Ni_2P(0001)$ surface and $*CH_3$ become the most stable species on the surface in this case.

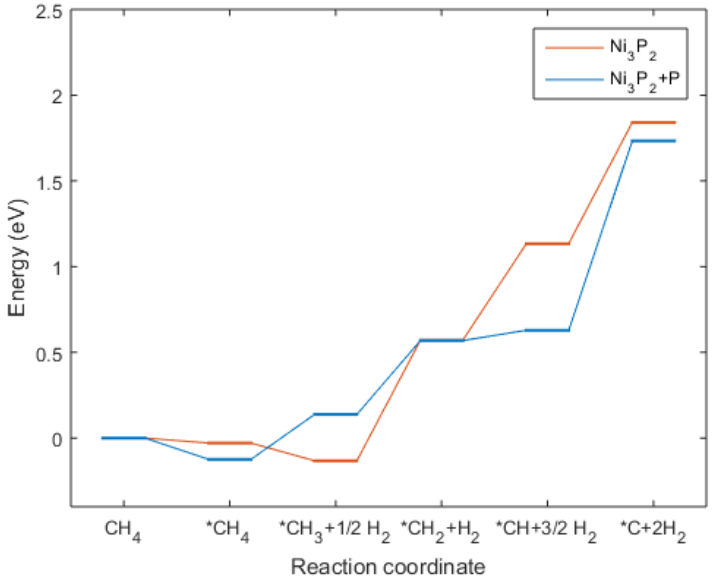

Fig. 5 Potential energy diagram for CH_4 dissociation on Ni_3P_2-terminated and Ni_3P_2+P-terminated $Ni_2P(0001)$ surfaces.

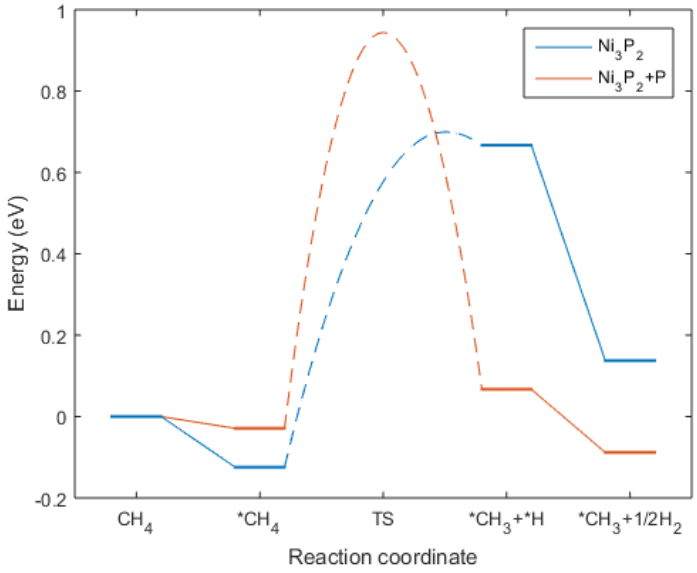

Fig. 6 Potential energy diagram for $CH_4 \rightarrow CH_3 + H$ on Ni_3P_2-terminated and Ni_3P_2+P-terminated $Ni_2P(0001)$ surfaces.

Going from thermodynamics, we now study the kinetics of the first C-H bond cleavage of CH_4: $* CH_4 \rightarrow * CH_3 + * H$, which has been identified as the activity-controlling step for Ni-based

catalysts for CH_4 activation.[21, 72-74] As shown in Fig. 6, the reaction is slightly endothermic (0.14 eV). In the initial state, CH_4 interacts weakly with the Ni_3P_2-terminated surface, where the molecule is away from the surface (Fig. 7a). The final state includes the strongly adsorbed $*CH_3$ on the Ni_3 hollow sites and *H at the neighboring Ni-P bridge site (Fig. 7a), which eventually desorb as H_2. The transition state corresponds to the approaching of CH_4 approaches to the surface Ni_3 sites or an early transition, where the carbon atom shifts toward the Ni-Ni bridge site and two hydrogen atoms are pushed onto Ni atop. It results in an activation barrier of 0.82 eV, which is slightly lower than the previously reported for Ni(111) (1.04 eV[72], or 0.93 eV[74]). That is, Ni_3P_2-terminated Ni_2P(0001) surface can display the potential to activate CH_4 more efficiently than Ni(111).

On Ni_3P_2+P-terminated surface, the initial state is similar as the case of Ni_3P_2-terminated surface, where CH_4 is physisorbed (Fig. 7b). The final state in this case is only associated with the single P-II site, which provides binding to both $*CH_3$ and *H and the formation of methylphosphine molecule (CH_3PH), a crucial atmospheric tracer gasses in the atmosphere of Giant planets.[75] The transition state corresponds to a late transition, where the C-H bond is potentially elongated in interacting with P-II. Although the reaction is slightly exothermic on Ni_3P_2+P-terminated surface (Fig. 6), the corresponding barrier (0.95 eV) is slightly higher than that on Ni_3P_2-terminated Ni_2P(0001) surface; yet it is still comparable with that of Ni(111). The single site mediated by P-II allows the lower barrier for the C-H bond cleavage than that via the multiple sites (barrier 2.94 eV), where Ni-P bridge sites also participates in stabilizing *H. Such single site catalysis for CH_4 activation has been reported for oxygen [21, 33] on metal surfaces or on oxide. This is the first time reported for Phosphorus. Note that such catalytic capability is only observed for P-II rather than P-I. This is due to the unique electronic property of (Fig. 3b) and structural motif of P-II, which not only facilitates the approach of CH_4 with strong electrostatic attraction and little steric repulsion, but also allows the electron transfer required for C-H bond cleavage.

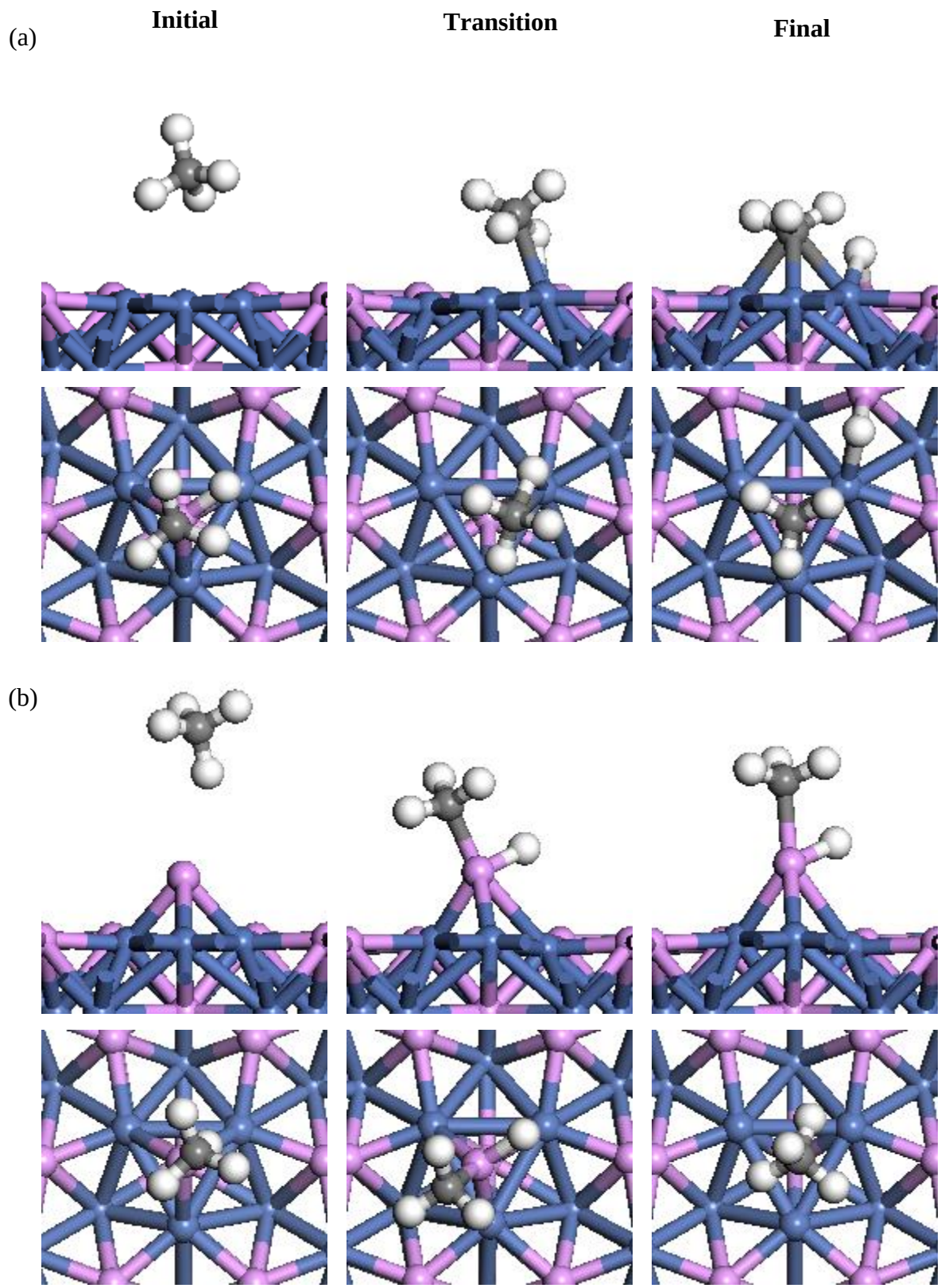

Fig. 7 Side and top view of initial, transition and final states for CH_4 dissociation on (a) Ni_3P_2-terminated and (b) Ni_3P_2+P-terminated $Ni_2P(0001)$ surfaces. White: H; Grey: C; Purple: P; Blue: Ni.

Compared with the previous results on Ni(111) and Ni(211) (Table 4), the first C-H bond cleavage on $Ni_2P(0001)$ surface is less endothermic, while the rest of dissociations are more endothermic. The first and the last C-H bond breakings are the most difficult steps of CH_4 dissociation on Ni surfaces, yet this does not seem to be the case on the Ni_2P surface, where only the formation of *C is highly endothermic. However, as shown in the following, CH_4 dissociation is not likely to occur on Ni_2P in the presence of H_2O under the reforming conditions.

Table 4 Reaction energies (eV) on Ni_3P_2+P-terminated and Ni_3P_2+P-terminated $Ni_2P(0001)$ surface in comparison of Ni(111) and Ni(211)*

	$CH_4\rightarrow$ $*CH_3+½H_2$	$*CH_3\rightarrow$ $*CH_2+½H_2$	$*CH_2\rightarrow$ $*CH+½H_2$	$*CH\rightarrow$ $*C+½H_2$	$H_2O\rightarrow$ $*OH+½H_2$	$*OH\rightarrow$ $*O+ ½H_2$
Ni_2P	0.47	0.71	0.31	1.36	-0.35	0.73
Ni_2P+P	0.13	1.31	0.53	1.48	-0.27	0.02
Ni(111)	0.98	0.54	0.07	1.05	0.29	0.16
Ni(211)	0.75	0.45	0.03	0.13	-0.23	0.90

* The results for Ni(111) and Ni(211) were cited from ref. [72].

3.3.2 Water Dissociation

Although $Ni_2P(0001)$ surface is able to activate CH_4 as that of Ni, it is not clear how it competes with the H_2O adsorption and dissociation under the reforming conditions. In this section, complete H_2O dissociation was investigated: $* H_2O \rightarrow * OH + * H$, $* OH \rightarrow * O + * H$.

Partial and complete H_2O dissociations on both Ni_3P_2-terminated and Ni_3P_2+P-terminated $Ni_2P(0001)$ surfaces are exothermic (Fig. 8). With Ni_3P_2 termination, H_2O molecular adsorbs on Ni atop site as initial state (Fig. 9a). The final state for the first O-H bond cleavage involves *OH at the Ni_3 hollow sites and *H at the neighboring Ni-P bridge sites, which eventually desorbs as H_2. A late transition is observed over the Ni_3 site, where one of O-H bond is elongated. The corresponding barrier is 0.59 eV. With Ni_3P_2+P termination, the initial H_2O adsorption is as weak as CH_4, though the final state is energetically comparable with that on the Ni_3P_2-termination (Fig. 8), where *OH and *H adsorbs at P-II top site and P-I top site respectively together with significant displacement of P outward the surface (Fig. 9b). The transition state represents a stretched O-H bond over the P-II-P-I bridge site, which is associated with a slightly lower barrier (0.57 eV) than that on the Ni_3P_2 termination.

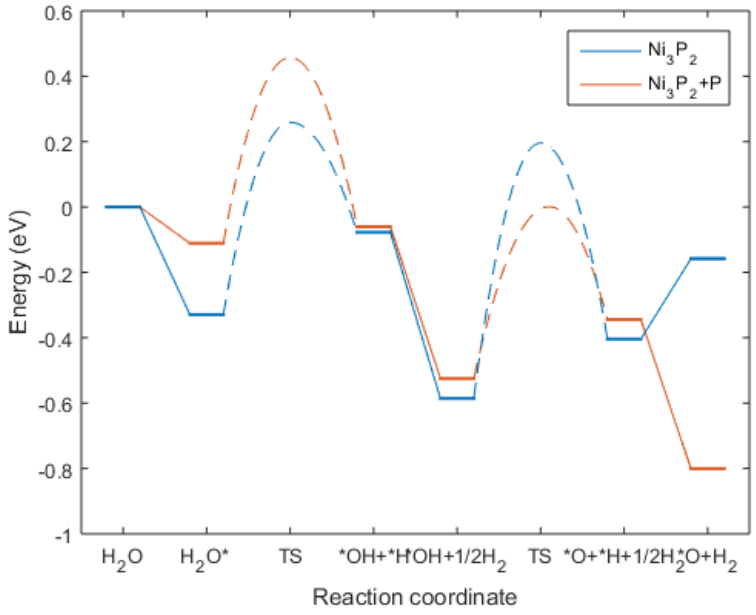

Fig. 8 Potential energy diagram for H_2O dissociation on Ni_3P_2-terminated and Ni_3P_2+P-terminated $Ni_2P(0001)$ surfaces.

The second O-H bond cleavage on Ni_3P_2-terminated surface involves the shift of *OH from the initial Ni_3 site to the neighboring Ni-P bridge site as a transition (Fig. 10a). The final state includes *O at the Ni-P bridge site and *H at the Ni_3 hollow sites. With such shift of *OH, the barrier for O-H cleavage is 0.78 eV, which is 0.72 eV lower than the case where both *OH and *O stay at the Ni_3 site (Fig. 8). The reason is that nickel hollow is active site for O-H bond break. This is due to the big difference in site preference for *O and *H. For *O (Table 2), the Ni_3 site is as active as the Ni-P bridge site, while in the case of *H, the Ni_3 site is strongly favored. As a result, the swap in position of dissociated *O from Ni_3 to Ni-P site and *H from Ni-P to Ni_3 site results the energy gain in the final state by about 0.8 eV (Fig. 8) and therefore a lowered barrier.

By comparison, the second O-H bond cleavage on Ni_3P_2+P termination is more straightforward. The transition state corresponds to a tilting of *OH from the initial P-II top site toward the neighboring P-I site with a weak H-P bond formed (Fig. 10b). The O-H bond broken results in the final state, including *O staying at the top of P-II as *OH, and *H occupying the Ni-P bridge site (Fig. 10b). The corresponding barrier is 0.53 eV, which is slightly lower than that on the Ni_3P_2 termination.

(a) **Initial** **Transition** **Final**

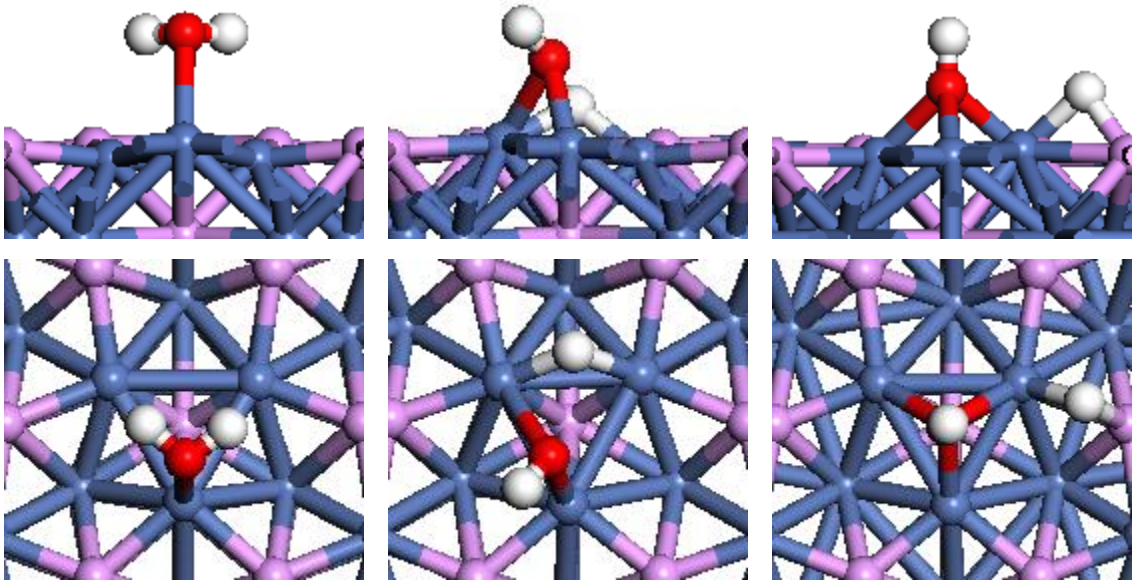

(b)

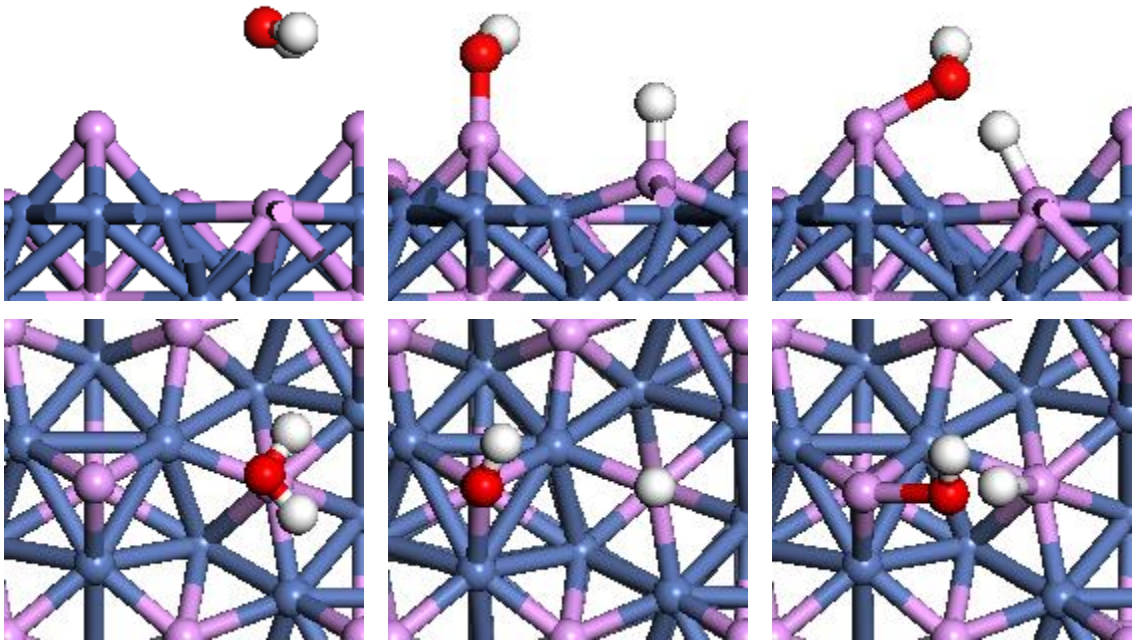

Fig. 9 Side and top view of initial, transition and final states for $* H_2O \rightarrow * OH + * H$, on (a) Ni_3P_2-terminated and (b) Ni_3P_2+P-terminated $Ni_2P(0001)$ surfaces. White: H; Red: O; Purple: P; Blue: Ni.

(a)

Initial **Transition** **Final**

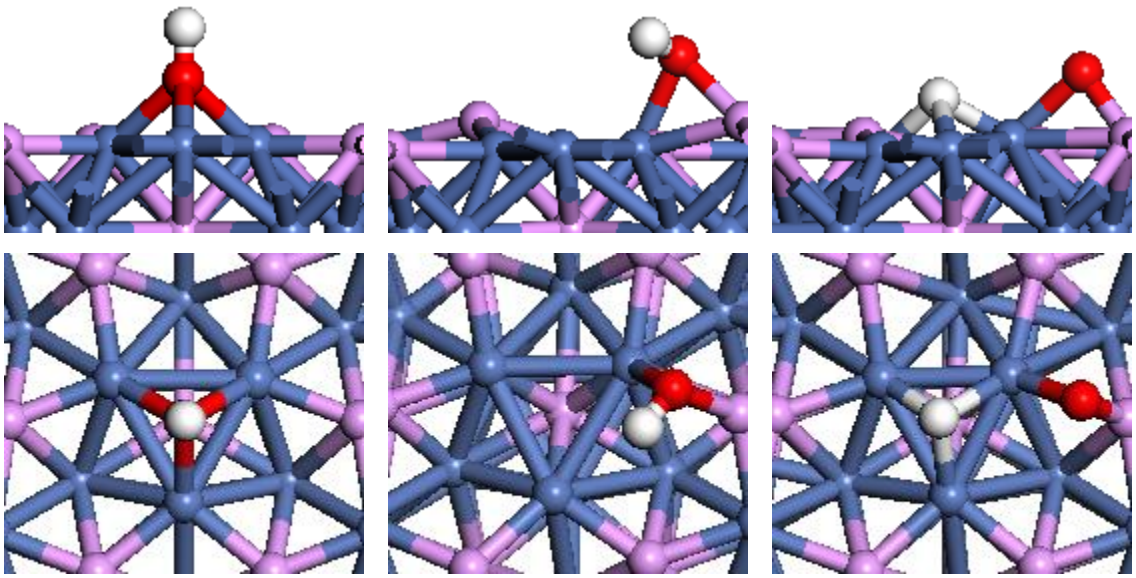

(b)

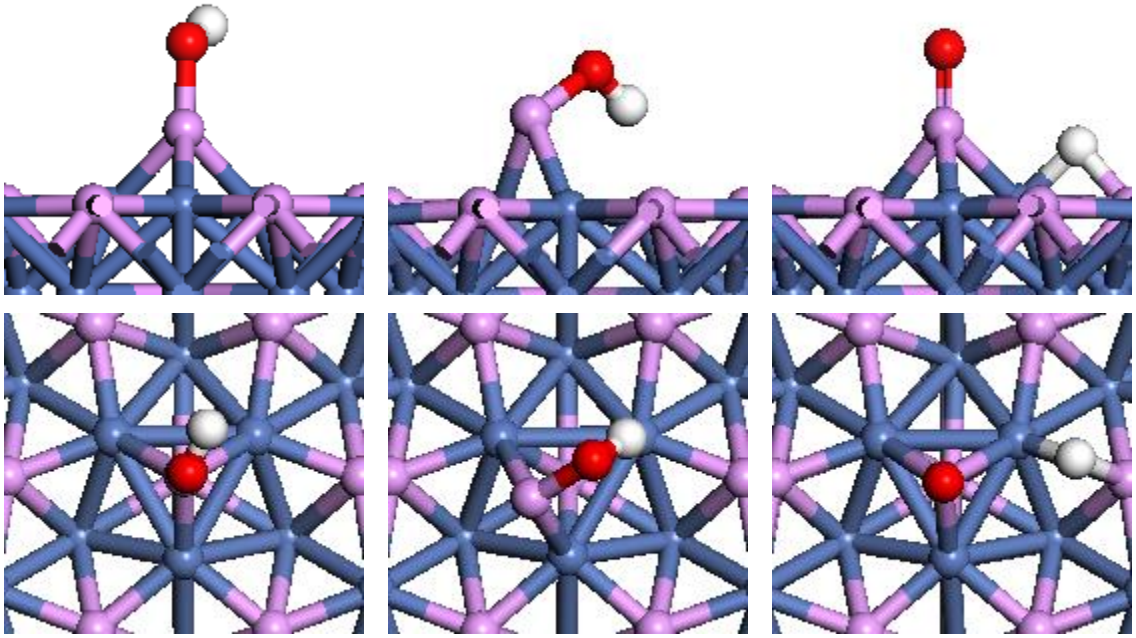

Fig. 10 Side and top view of initial, transition and final states for $* OH \rightarrow * O + * H$ (a) Ni_3P_2-terminated and (b) Ni_3P_2+P-terminated $Ni_2P(0001)$ surfaces. White: H; Red: O; Purple: P; Blue: Ni.

As demonstrated above, the H_2O dissociation on both terminations is energetically comparable, and is more preferential than CH_4 dissociation. We note that both reactions compete for the same type of sites on the surfaces: Ni_3 and Ni-P bridge sites on the Ni_3P_2 termination and P-II sites on the Ni_3P_2+P termination. That is, H_2O dissociation is preferred over CH_4 dissociation, and the active sites on both surface terminations are likely to be covered by the dissociated fragments from H_2O dissociation, which may eventually enable CH_4 activation. This is different from pure Ni, where barriers for CH_4 and H_2O dissociations are comparable, and difficult step is to remove *CH or *C from the surface via oxidaiton.[72]

In comparison with pure Ni (Table 4), the Ni_3P_2-terminated surface behaves similarly as Ni(211), where the first O-OH bond cleavage is more favorable than the second, while for Ni(111), they are energetically comparable. On the Ni_3P_2+P-terminated surface, the formation of *O is as favorable as that of *OH, due to the selectively stabilization of *O on the P-II site.

As shown in Fig. 8, both *OH and *O can be stabilized as surface species during H_2O dissociation. Now the question is whether these stable species can lead to the surface poisoning. To answer that, we calculated the adsorptions of *OH and *O on both Ni_3P_2-terminated and Ni_3P_2+P-terminated $Ni_2P(0001)$ surfaces at different coverage. The adsorption energy was calculated as

$$E_{nX} = E(n * X) - \mathrm{E}[(n-1) * X] - E(X) \quad (6)$$

where n is the number of adsorbates *X in a supercell.

On the Ni_3P_2-terminated surface, *OH strongly prefers the Ni_3 site at coverage of 1/3 monolayer (ML) with adsorption energy of -0.59 eV (Fig. 11a). With the coverage increasing to 2/3 ML and 1 ML, the Ni-P bridge sites are occupied, and the corresponding binding is significantly weakened to -0.08 eV. The increase of coverage to 4/3 ML of coverage is highly unfavorited, where the adsorption at the P atop sites corresponds to a positive adsorption energy of 0.36 eV. The adsorption of *O is more complex compared to *OH. At 1/3 ML, the adsorptions on the Ni_3 and Ni-P bridge sites are almost the same in energy. If the Ni_3 sites are occupied first, the further adsorption of *O is energetically unfavorable; while if one of the Ni-P sites are occupied first, the coverage increasing to 1ML by occupying all Ni-P sites is also possible, though the corresponding adsorptions are not as strong as the first (Fig. 11b). Given that, the produced *OH species are likely only occupy the Ni_3 sites and reaches to the coverage

of 1/3 ML, while the *O species prefer to occupy all Ni-P bridge sites with the coverage approaching to 1 ML.

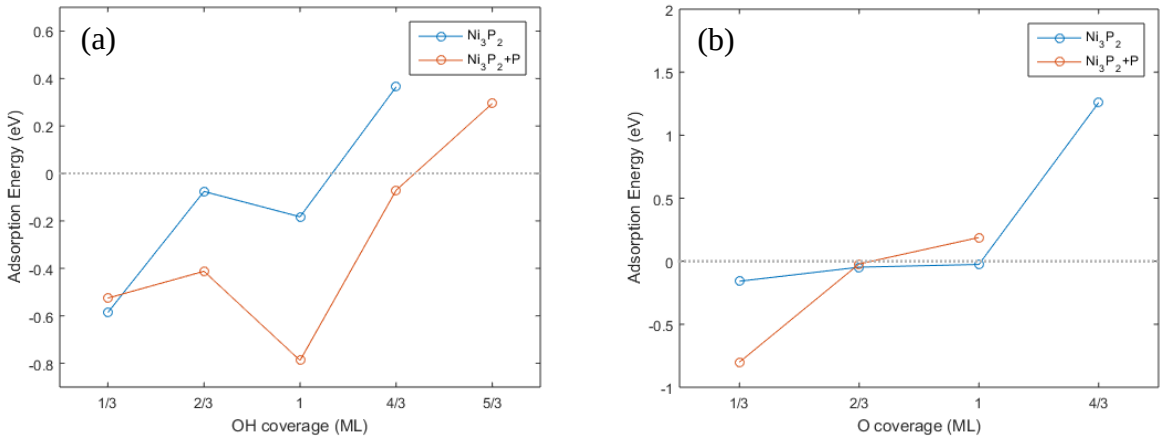

Fig. 11 Calculated adsorption energies of (a) *OH and (b) *O on both Ni_3P_2-terminated and Ni_3P_2+P-terminated $Ni_2P(0001)$ surfaces at different coverage.

On Ni_3P_2+P-terminated surface, the P-II site plays an important role. For *OH, the strongest adsorption is observed at 1/3 ML at P-II top sites with the adsorption energy of -0.53 eV. Increasing the coverage to 2/3 ML results in the adsorption energy increase to -0.69 eV, yet the corresponding adsorption site is also P-II top. At higher coverage, the binding of *OH is significantly reduced to -0.50 eV at 1 ML, -0.07 eV at 4/3 ML and +0.29 eV at 5/3 ML (Fig. 11a). The resulted motif corresponds to each P-II site saturated by three *OH and each P-I site occupied by one *OH. According to the energetics, the surface with each P-II atom can be saturated by at two or three *OH together with the slightly shifts of P-II to nickel atop (0.88 Å). It suggests that P-II may not be stable and can be removed from the surface by heavy oxidation. However, as H_2O dissociates at the P-II site, as shown above and the hydroxylation of P-II will hinder the further adsorption and dissociation of H_2O. Therefore, by comparison *OH at the P-II site with coverage of 1/3 ML is more likely. If *O species are produced, Fig. 11b clearly shows that the coverage can only reach 1/3 ML with one *O adsorbed at the top of P-II and adsorption energy of -0.15 eV, while the additional *O at P-II top site (2/3 ML) or Ni-P bridge site (1 ML) do not bind well with the surface.

According to our results on the adsorption of *OH and *O on both Ni_3P_2-terminated and Ni_3P_2+P-terminated $Ni_2P(0001)$ surfaces, we will study in the next CH_4 dissociation on *OH- and *O-precovered surfaces.

*3.3.3 Methane Activation by *OH*

According to the results shown in Section 3.3.2, *OH at coverage of 1/3ML on the $Ni_2P(0001)$ surface with both terminations is energetically likely. On Ni_3P_2-terminated surface, *OH occupies the Ni_3 hollow sites. On the *OH-precovered surface CH_4 does not adsorb as the active Ni_3 site is occupied by *OH. The first C-H bond cleavage produces CH_3OH and removes *OH from the Ni_3 sites (Fig. 12a). This reaction is highly endothermic with reaction energy of 1.09 eV and highly activated with a barrier of 1.69 eV. The transition state corresponds to CH_4 dumps one hydrogen to the Ni-P site and the produced $*CH_3$ approaches to the *OH to form CH_3OH.

In comparison, CH_4 reforming to CH_3OH on the Ni_3P_2+P-terminated surface covered by *OH at P-II sites is easier, corresponding to a barrier of 1.24 eV, though the reaction energy is similar (1.03 eV). The similarity in reaction energy is due to the weakly-bound CH_4 and CH_3OH as the case of Ni_3P_2+P-terminatated surface, while the difference in activation barrier is associated the variation in reaction mechanism. As Fig. 12b, on the Ni_3P_2+P termination, CH_4 reforming is mediated by formation of H_2O, where CH_4 transfers one hydrogen to *OH first and the formed H_2O rotates to produce CH_3OH and leave one hydrogen atom at the top of P-II.

We note that in both cases the reverse reaction, CH_3OH dissociation, is more favorable than the forward reaction due to the high endothermicity of the reaction. As a result, the formation of CH_3OH can be hindered by the facile reverse reaction. To avoid that, the high pressure of CH_4 may be required to tune the equilibrium more toward CH_3OH formation. Nevertheless, the barriers for the forward reaction on both terminations are still high and the CH_3OH formation via CH_4 activation by *OH can be difficult.

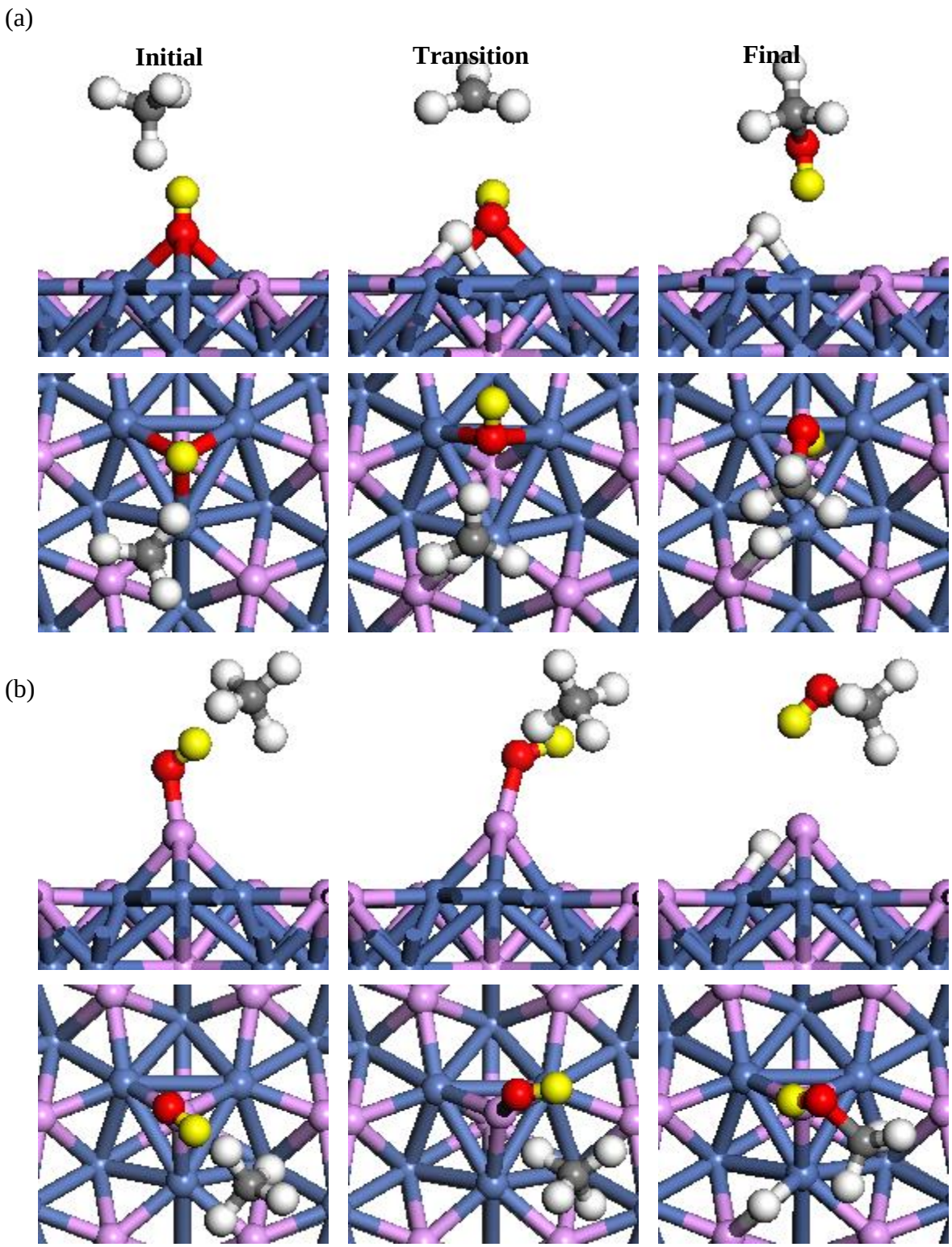

Fig. 12 Side and top view of initial, transition and final states for $CH_4 + *\,\mathrm{OH} \rightarrow CH_3\mathrm{OH} + *\,\mathrm{H}$ on (a) Ni_3P_2-terminated and (b) Ni_3P_2+P-terminated $Ni_2P(0001)$ surfaces. White: H; yellow: H on hydroxyl; Red: O; Grey: C; Purple: P; Blue: Ni.

*3.3.4 Methane Activation by *O*

In Section 3.2, our results show that there are two stable sites on Ni_3P_2-terminated $Ni_2P(0001)$ surface for *O adsorption: Ni_3 hollow and Ni-P bridge sites. According to the calculations shown in Section 3.3.2, the maximum coverage for *O is 1/3 ML if *O occupies the Ni_3 site first, and 1 ML is also likely to be reached if the Ni-P bridge site is considered, though the preference for the 2/3 ML and 1 ML is not as strong as that for 1/3 ML. Accordingly, we calculated the barrier for CH_4 reforming to CH_3OH on *O at both Ni_3 site and Ni-P bridge site at coverage of 1/3ML. The reaction involves the direct dissociation of CH_4 at the *O site, which produces CH_3OH and generates an oxygen vacancy. Our results show that the reaction is endothermic with the reaction energy of 0.67 eV. Both CH_4 and CH_3OH weakly interact with the surface (Fig. 13a). The reaction on *O shows different mechanism from that on *OH. The transition state corresponds to an early transition, where CH_4 approaches to *O with a stretched C-H bond (Fig. 13a). The position of *O indeed affects the reaction barrier. When *O is located at the Ni_3 hollow site, the activation barrier is 1.27 eV, while it is lowered to 1.06 eV on moving from the Ni_3 hollow site to the Ni-P bridge site. This is, CH_4 reforming to CH_3OH in presence of *O is more preferential than that on *OH and is likely to occur under the reforming conditions with the temperature raised to 400-500 K.[36]

In comparison, the reaction on the *O-precovered Ni_3P_2+P-terminated surface is more difficult, where the reaction is more endothermic with the reaction energy of 1.31 eV and the corresponding barrier is increased to 1.56 eV. The transition state corresponds to a product-like late transition, where *O has been pulled away from the surface to break C-H bond and form CH_3OH (Fig. 13b). Therefore, CH_4 reforming to CH_3OH can be hindered with the extra P-II presence on the surface of $Ni_2P(0001)$. Different from the case of Ni_3P_2 termination, the surface *OH is more active than *O. This is due to higher stability of *O on the Ni_3P_2+P-termination than that on the Ni_3P_2-termination and *OH on the surface, making the removal of *O from the surface more difficult. Similar to the reforming by *OH, in the case of *O the barrier for the CH_3OH formation is higher than the reverse due to the endothermicity of the reaction. This, the high pressure for CH_4 is also necessary to enable to reaction to occur.

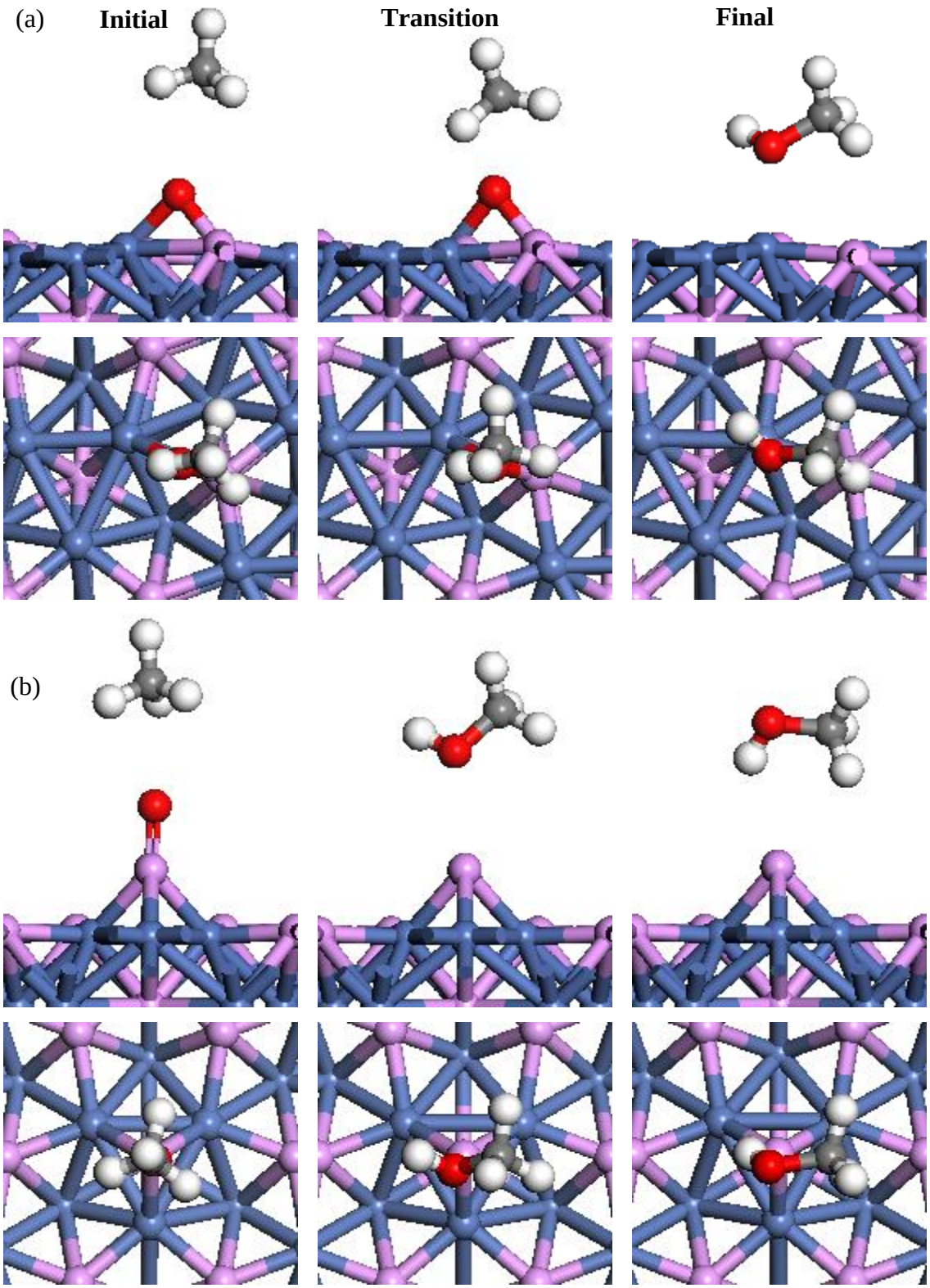

Fig. 13 Side and top view of initial, transition and final states for $CH_4 + * OH \rightarrow CH_3OH + * H$ on (a) Ni_3P_2-terminated and (b) Ni_3P_2+P-terminated $Ni_2P(0001)$ surfaces. White: H; Red: O; Grey: C; Purple: P; Blue: Ni.

Direct CH_4 reforming to CH_3OH has been previously observed on metal oxide systems.[24, 32-36] Our study is the first time to report the catalytic potential of Ni oxyphosphide for this reaction. In the next step, we will be working with our experimental collaborators to validate our theoretical prediction.

4. Conclusion

Methane activations were studied on a model $Ni_2P(0001)$ surface using DFT. Two types of terminations, Ni_3P_2 and Ni_3P_2+ P, were considered. The adsorptions of various reaction intermediates involved in methane activation were investigated. On the Ni_3P_2-terminated surface, Ni_3 sites are active to stabilize most of the reaction intermediates, while the P sites also participates in the binding directly and provides strong bindings to the species like *O and *CH_2. On the Ni_3P_2+ P-terminated surface, although the active Ni hollow sites are blocked by an extra P, the P adatom forms a new active site by itself, being able to selectively stabilize the *CH_3 and *O species on the surface compared to that on the Ni_3P_2-termination; however, for the other intermediates, the bindings are either weakened or slightly affected.

The formation of Ni_2P can tune the mechanism of methane reforming reaction on Ni completely. On pure Ni, C-H bond breaking of methane is facile, and CO is likely to be produced. The drawback, though, is the problematic removal of *CH or *C due to their high stability. In the case of Ni_2P, methane dissociation cannot compete with water dissociation. As a result, the active sites on the surface are likely covered by either *OH or *O from water dissociation. Our DFT calculations show that such surface species can be active to activate methane via direct dissociation to produce methanol together with the removal of *O. In this case, there is not obvious surface poisoning observed. Among the systems studied, *O at the Ni-P bridge site of Ni_3P_2-terminated $Ni_2P(0001)$ surface displays the highest activity toward C-H bond breaking and direct formation of methanol; by comparison, *O on Ni_3P_2+P-terminated surface is less active and the reaction on *OH on both terminations is more difficult.

Overall, the formation of phosphides hinders the CO formation on pure Ni, while it opens a new route toward direct methane activation to methanol, an economical way to obtain valuable chemicals directly from abundant natural gas resources as it can eliminate the need for expensive steam reforming. It also hinders the surface poisoning, which is a big challenge for Ni catalysts. The unique catalytic behavior of Ni_2P during methane reforming is associated with the synergy between Ni and P sites. On one hand, the coordination between Ni_3 hollow sites and Ni-P hybrid sites on $Ni_2P(0001)$ surface selectively promotes complete water dissociation rather than methane dissociation; on the other hand, it generates a new active sites, *O at Ni-P bridge sites, being able to not only release the carbon deposition on Ni catalysts, but also activate methane for direct methanol production.

References

1. Horn, R.; Schlögl, R., Methane Activation by Heterogeneous Catalysis. *Catalysis Letters* **2015**, *145*, 23-39.
2. Tang, P.; Zhu, Q.; Wu, Z.; Ma, D., Methane Activation: The Past and Future. *Energy & Environmental Science* **2014**, *7*, 2580-2591.
3. Lide, D.; Haynes, W., *Crc Handbook of Chemistry and Physics: A Ready-Reference Book of Chemical and Physical Data-/Editor-in-Chief, David R. Lide; Ass. Ed. Wm" Mickey" Haunes*; Boca Raton, Fla: CRC, 2009.
4. Liander, H., The Utilisation of Natural Gases for the Ammonia Process. *Transactions of the Faraday Society* **1929**, *25*, 462-472.
5. Rostrup-Nielsen, T., Manufacture of Hydrogen. *Catalysis Today* **2005**, *106*, 293-296.
6. Freni, S.; Calogero, G.; Cavallaro, S., Hydrogen Production from Methane through Catalytic Partial Oxidation Reactions. *Journal of Power Sources* **2000**, *87*, 28-38.
7. Sabatier, P.; Senderens, J.-B., Nouvelles Syntheses Du Methane. *Compt. Rend* **1902**, *134*, 514-516.
8. Sabatier, P.; Senderens, J., Direct Hydrogenation of Oxides of Carbon in Presence of Various Finely Divided Metals. *CR Acad Sci* **1902**, *134*, 689-691.
9. Fan, X.; Liu, Z.; Zhu, Y.-A.; Tong, G.; Zhang, J.; Engelbrekt, C.; Ulstrup, J.; Zhu, K.; Zhou, X., Tuning the Composition of Metastable Coxniymg100−X−Y(Oh)(Och3) Nanoplates for Optimizing Robust Methane Dry Reforming Catalyst. *J. Catal.* **2015**, *330*, 106-119.
10. Pakhare, D.; Spivey, J., A Review of Dry (Co2) Reforming of Methane over Noble Metal Catalysts. *Chem. Soc. Rev.* **2014**, *43*, 7813-7837.
11. Zuo, Z.-J.; Shen, C.-F.; Tan, P.-J.; Huang, W., Ni Based on Dual-Support Mg-Al Mixed Oxides and Sba-15 Catalysts for Dry Reforming of Methane. *Catal. Commun.* **2013**, *41*, 132-135.
12. Wang, J.; Sun, Q.; Chan, S.; Su, H., The Acceleration of Methanol Synthesis and C2 Oxygenates Formation on Copper Grain Boundary from Syngas. *Appl. Catal. A* **2016**, *509*, 97-104.
13. Delgado, J. A.; Castillón, S.; Curulla-Ferré, D.; Claver, C.; Godard, C., Effect of Ph on Catalyst Activity and Selectivity in the Aqueous Fischer–Tropsch Synthesis Catalyzed by Cobalt Nanoparticles. *Catal. Commun.* **2015**, *71*, 88-92.
14. Zuo, Z.-J.; Wang, L.; Yu, L.-M.; Han, P.-D.; Huang, W., Experimental and Theoretical Studies of Ethanol Synthesis from Syngas over Cuznal Catalysts without Other Promoters. *J. Phys. Chem. C* **2014**, *118*, 12890-12898.

15. Figen, H. E.; Baykara, S. Z., Hydrogen Production by Partial Oxidation of Methane over Co Based, Ni and Ru Monolithic Catalysts. *International Journal of Hydrogen Energy* **2015**, *40*, 7439-7451.
16. Studt, F., et al., The Mechanism of Co and Co2 Hydrogenation to Methanol over Cu-Based Catalysts. *ChemCatChem* **2015**, *7*, 1105-1111.
17. Mehta, D. U.; Khirsariya, P.; Mewada, R. K., Chemical, Civil and Mechanical Engineering Tracks of 3rd Nirma University International Conference on Engineering (Nuicone2012)Single Step Oxidation of Methane to Methanol–Towards Better Understanding. *Procedia Engineering* **2013**, *51*, 409-415.
18. Shiota, Y.; Yoshizawa, K., Methane-to-Methanol Conversion by First-Row Transition-Metal Oxide Ions: Sco+, Tio+, Vo+, Cro+, Mno+, Feo+, Coo+, Nio+, and Cuo+. *Journal of the American Chemical Society* **2000**, *122*, 12317-12326.
19. Han, B.; Yang, Y.; Xu, Y.; Etim, U.; Qiao, K.; Xu, B.; Yan, Z., A Review of the Direct Oxidation of Methane to Methanol. *Chinese Journal of Catalysis* **2016**, *37*, 1206-1215.
20. Periana, R. A.; Bhalla, G.; Tenn, W. J.; Young, K. J.; Liu, X. Y.; Mironov, O.; Jones, C.; Ziatdinov, V. R., Perspectives on Some Challenges and Approaches for Developing the Next Generation of Selective, Low Temperature, Oxidation Catalysts for Alkane Hydroxylation Based on the Ch Activation Reaction. *Journal of Molecular Catalysis A: Chemical* **2004**, *220*, 7-25.
21. Latimer, A. A.; Kulkarni, A. R.; Aljama, H.; Montoya, J. H.; Yoo, J. S.; Tsai, C.; Abild-Pedersen, F.; Studt, F.; Norskov, J. K., Understanding Trends in C-H Bond Activation in Heterogeneous Catalysis. *Nat Mater* **2017**, *16*, 225-229.
22. Starokon, E. V.; Parfenov, M. V.; Arzumanov, S. S.; Pirutko, L. V.; Stepanov, A. G.; Panov, G. I., Oxidation of Methane to Methanol on the Surface of Fezsm-5 Zeolite. *Journal of Catalysis* **2013**, *300*, 47-54.
23. Khirsariya, P.; Mewada, R. K., Single Step Oxidation of Methane to Methanol–Towards Better Understanding. *Procedia Engineering* **2013**, *51*, 409-415.
24. Grundner, S.; Markovits, M. A. C.; Li, G.; Tromp, M.; Pidko, E. A.; Hensen, E. J. M.; Jentys, A.; Sanchez-Sanchez, M.; Lercher, J. A., Single-Site Trinuclear Copper Oxygen Clusters in Mordenite for Selective Conversion of Methane to Methanol. *Nature Communications* **2015**, *6*, 7546.
25. Chin, Y.-H.; Buda, C.; Neurock, M.; Iglesia, E., Consequences of Metal–Oxide Interconversion for C–H Bond Activation During Ch4 Reactions on Pd Catalysts. *Journal of the American Chemical Society* **2013**, *135*, 15425-15442.
26. Aasberg-Petersen, K.; Dybkjær, I.; Ovesen, C.; Schjødt, N.; Sehested, J.; Thomsen, S., Natural Gas to Synthesis Gas–Catalysts and Catalytic Processes. *Journal of Natural Gas Science and Engineering* **2011**, *3*, 423-459.

27. German, E. D.; Sheintuch, M., Predicting Ch4 Dissociation Kinetics on Metals: Trends, Sticking Coefficients, H Tunneling, and Kinetic Isotope Effect. *The Journal of Physical Chemistry C* **2013**, *117*, 22811-22826.
28. Wang, B.; Albarracín-Suazo, S.; Pagán-Torres, Y.; Nikolla, E., Advances in Methane Conversion Processes. *Catalysis Today* **2017**, *285*, 147-158.
29. Banerjee, R.; Proshlyakov, Y.; Lipscomb, J. D.; Proshlyakov, D. A., Structure of the Key Species in the Enzymatic Oxidation of Methane to Methanol. *Nature* **2015**, *518*, 431-434.
30. Chan, S. I.; Yu, S. S. F., Controlled Oxidation of Hydrocarbons by the Membrane-Bound Methane Monooxygenase: The Case for a Tricopper Cluster. *Accounts of Chemical Research* **2008**, *41*, 969-979.
31. Olivos-Suarez, A. I.; Szécsényi, À.; Hensen, E. J. M.; Ruiz-Martinez, J.; Pidko, E. A.; Gascon, J., Strategies for the Direct Catalytic Valorization of Methane Using Heterogeneous Catalysis: Challenges and Opportunities. *ACS Catalysis* **2016**, *6*, 2965-2981.
32. Li, G.; Vassilev, P.; Sanchez-Sanchez, M.; Lercher, J. A.; Hensen, E. J. M.; Pidko, E. A., Stability and Reactivity of Copper Oxo-Clusters in Zsm-5 Zeolite for Selective Methane Oxidation to Methanol. *Journal of Catalysis* **2016**, *338*, 305-312.
33. Göltl, F.; Michel, C.; Andrikopoulos, P. C.; Love, A. M.; Hafner, J.; Hermans, I.; Sautet, P., Computationally Exploring Confinement Effects in the Methane-to-Methanol Conversion over Iron-Oxo Centers in Zeolites. *ACS Catalysis* **2016**, *6*, 8404-8409.
34. Hammond, C., et al., Direct Catalytic Conversion of Methane to Methanol in an Aqueous Medium by Using Copper-Promoted Fe-Zsm-5. *Angewandte Chemie International Edition* **2012**, *51*, 5129-5133.
35. Zhao, Z.-J.; Kulkarni, A.; Vilella, L.; Nørskov, J. K.; Studt, F., Theoretical Insights into the Selective Oxidation of Methane to Methanol in Copper-Exchanged Mordenite. *ACS Catalysis* **2016**, *6*, 3760-3766.
36. Zuo, Z.; Ramírez, P. J.; Senanayake, S. D.; Liu, P.; Rodriguez, J. A., Low-Temperature Conversion of Methane to Methanol on Ceox/Cu2o Catalysts: Water Controlled Activation of the C–H Bond. *Journal of the American Chemical Society* **2016**, *138*, 13810-13813.
37. Rostrupnielsen, J.; Hansen, J. B., Co2-Reforming of Methane over Transition Metals. *Journal of Catalysis* **1993**, *144*, 38-49.
38. Menezes, P. W.; Indra, A.; Littlewood, P.; Göbel, C.; Schomäcker, R.; Driess, M., A Single-Source Precursor Approach to Self-Supported Nickel–Manganese-Based Catalysts with Improved Stability for Effective Low-Temperature Dry Reforming of Methane. *ChemPlusChem* **2016**, n/a-n/a.

39. Luisetto, I.; Tuti, S.; Battocchio, C.; Lo Mastro, S.; Sodo, A., Ni/Ceo2–Al2o3 Catalysts for the Dry Reforming of Methane: The Effect of Cealo3 Content and Nickel Crystallite Size on Catalytic Activity and Coke Resistance. *Appl. Catal. A* **2015**, *500*, 12-22.
40. Li, Y.; Li, D.; Wang, G., Methane Decomposition to Cox-Free Hydrogen and Nano-Carbon Material on Group 8–10 Base Metal Catalysts: A Review. *Catal. Today* **2011**, *162*, 1-48.
41. Hou, Z.; Gao, J.; Guo, J.; Liang, D.; Lou, H.; Zheng, X., Deactivation of Ni Catalysts During Methane Autothermal Reforming with Co2 and O2 in a Fluidized-Bed Reactor. *J. Catal.* **2007**, *250*, 331-341.
42. Lercher, J.; Bitter, J.; Hally, W.; Niessen, W.; Seshan, K., Design of Stable Catalysts for Methane-Carbon Dioxide Reforming. *Studies in Surface Science and Catalysis* **1996**, *101*, 463-472.
43. Abild-Pedersen, F.; Nørskov, J. K.; Rostrup-Nielsen, J. R.; Sehested, J.; Helveg, S., Mechanisms for Catalytic Carbon Nanofiber Growth Studied by Ab Initio Density Functional Theory Calculations. *Physical Review B* **2006**, *73*, 115419.
44. Rostrup-Nielsen, J., Sulfur-Passivated Nickel Catalysts for Carbon-Free Steam Reforming of Methane. *Journal of Catalysis* **1984**, *85*, 31-43.
45. Tomishige, K.; Himeno, Y.; Matsuo, Y.; Yoshinaga, Y.; Fujimoto, K., Catalytic Performance and Carbon Deposition Behavior of a Nio− Mgo Solid Solution in Methane Reforming with Carbon Dioxide under Pressurized Conditions. *Industrial & Engineering Chemistry Research* **2000**, *39*, 1891-1897.
46. Wang, S.-G.; Liao, X.-Y.; Hu, J.; Cao, D.-B.; Li, Y.-W.; Wang, J.; Jiao, H., Kinetic Aspect of Co2 Reforming of Ch4 on Ni(1 1 1): A Density Functional Theory Calculation. *Surface Science* **2007**, *601*, 1271-1284.
47. Rodriguez, J. A.; Kim, J.-Y.; Hanson, J. C.; Sawhill, S. J.; Bussell, M. E., Physical and Chemical Properties of Mop, Ni2p, and Monip Hydrodesulfurization Catalysts: Time-Resolved X-Ray Diffraction, Density Functional, and Hydrodesulfurization Activity Studies. *The Journal of Physical Chemistry B* **2003**, *107*, 6276-6285.
48. Oyama, S. T., Novel Catalysts for Advanced Hydroprocessing: Transition Metal Phosphides. *Journal of Catalysis* **2003**, *216*, 343-352.
49. Liu, P.; Rodriguez, J. A.; Asakura, T.; Gomes, J.; Nakamura, K., Desulfurization Reactions on Ni2p(001) and A-Mo2c(001) Surfaces: Complex Role of P and C Sites. *The Journal of Physical Chemistry B* **2005**, *109*, 4575-4583.
50. Liu, P.; Rodriguez, J. A., Catalysts for Hydrogen Evolution from the [Nife] Hydrogenase to the Ni2p (001) Surface: The Importance of Ensemble Effect. *Journal of the American Chemical Society* **2005**, *127*, 14871-14878.

51. Popczun, E. J.; McKone, J. R.; Read, C. G.; Biacchi, A. J.; Wiltrout, A. M.; Lewis, N. S.; Schaak, R. E., Nanostructured Nickel Phosphide as an Electrocatalyst for the Hydrogen Evolution Reaction. *Journal of the American Chemical Society* **2013**, *135*, 9267-9270.
52. Liu, P.; Rodriguez, J. A.; Takahashi, Y.; Nakamura, K., Water–Gas-Shift Reaction on a Ni 2 P (001) Catalyst: Formation of Oxy-Phosphides and Highly Active Reaction Sites. *Journal of catalysis* **2009**, *262*, 294-303.
53. Thomas, L. H. In *The Calculation of Atomic Fields*, Mathematical Proceedings of the Cambridge Philosophical Society, Cambridge Univ Press: 1927; pp 542-548.
54. Hohenberg, P.; Kohn, W., Inhomogeneous Electron Gas. *Physical review* **1964**, *136*, B864.
55. Hohenberg, P.; Kohn, W., Inhomogeneous Electron Gas. *Physical Review* **1964**, *136*, B864-B871.
56. Kresse, G.; Furthmüller, J., Efficient Iterative Schemes for Ab Initio Total-Energy Calculations Using a Plane-Wave Basis Set. *Physical review B* **1996**, *54*, 11169.
57. Perdew, J. P.; Wang, Y., Accurate and Simple Analytic Representation of the Electron-Gas Correlation Energy. *Physical Review B* **1992**, *45*, 13244-13249.
58. Kresse, G.; Joubert, D., From Ultrasoft Pseudopotentials to the Projector Augmented-Wave Method. *Physical Review B* **1999**, *59*, 1758.
59. Larsson, E., An X-Ray Investigation of Ni-P System and Crystal Structures of Nip and Nip2. *Arkiv for Kemi* **1965**, *23*, 335-&.
60. Lomnitskaya, Y. F.; Kuz'ma, Y. B., Study of the Niobium-Nickel-Phosphorus System. *INORGANIC MATER.* **1984**, *19*, 1191-1194.
61. Monkhorst, H. J.; Pack, J. D., Special Points for Brillouin-Zone Integrations. *Physical review B* **1976**, *13*, 5188.
62. Jónsson, H.; Mills, G.; Jacobsen, K. W., Nudged Elastic Band Method for Finding Minimum Energy Paths of Transitions. **1998**.
63. Cerjan, C. J.; Miller, W. H., On Finding Transition States. *The Journal of chemical physics* **1981**, *75*, 2800-2806.
64. Quapp, W., A Gradient-Only Algorithm for Tracing a Reaction Path Uphill to the Saddle of a Potential Energy Surface. *Chemical physics letters* **1996**, *253*, 286-292.
65. Taylor, H.; Simons, J., Imposition of Geometrical Constraints on Potential Energy Surface Walking Procedures. *Journal of Physical Chemistry* **1985**, *89*, 684-688.
66. Baker, J., An Algorithm for the Location of Transition States. *Journal of Computational Chemistry* **1986**, *7*, 385-395.

67. Mills, G.; Jónsson, H.; Schenter, G. K., Reversible Work Transition State Theory: Application to Dissociative Adsorption of Hydrogen. *Surface Science* **1995**, *324*, 305-337.
68. Li, Q.; Hu, X., First-Principles Study of Ni 2 P (0001) Surfaces. *Physical Review B* **2006**, *74*, 035414.
69. Moula, M.; Suzuki, S.; Chun, W. J.; Otani, S.; Oyama, S. T.; Asakura, K., Surface Structures of Ni2p (0001)—Scanning Tunneling Microscopy (Stm) and Low‐Energy Electron Diffraction (Leed) Characterizations. *Surface and interface analysis* **2006**, *38*, 1611-1614.
70. Wexler, R. B.; Martirez, J. M. P.; Rappe, A. M., Stable Phosphorus-Enriched (0001) Surfaces of Nickel Phosphides. *Chemistry of Materials* **2016**, *28*, 5365-5372.
71. Yuan, Q.; Ariga, H.; Asakura, K., An Investigation of Ni2p Single Crystal Surfaces: Structure, Electronic State and Reactivity. *Topics in catalysis* **2015**, *58*, 194-200.
72. Bengaard, H. S.; Nørskov, J. K.; Sehested, J.; Clausen, B. S.; Nielsen, L. P.; Molenbroek, A. M.; Rostrup-Nielsen, J. R., Steam Reforming and Graphite Formation on Ni Catalysts. *Journal of Catalysis* **2002**, *209*, 365-384.
73. Abild-Pedersen, F.; Lytken, O.; Engbæk, J.; Nielsen, G.; Chorkendorff, I.; Nørskov, J. K., Methane Activation on Ni(1 1 1): Effects of Poisons and Step Defects. *Surface Science* **2005**, *590*, 127-137.
74. Liu, B.; Lusk, M. T.; Ely, J. F., Influence of Nickel Catalyst Geometry on the Dissociation Barriers of H2 and Ch4: Ni13 Versus Ni(111). *The Journal of Physical Chemistry C* **2009**, *113*, 13715-13722.
75. Viana, R. B.; da Silva, A. B. F., The Ch3ph2 and Ch3ph Isomers: Isomerization, Hydrogen Release, Thermodynamic, and Spectroscopy Properties. *Journal of Molecular Modeling* **2014**, *20*, 2372.

Appendix

A. VASP INCAR input tags list

The calculation was performed with software VASP. In VASP, many parameters, methods and switches are input via INCAR file with a special format. To understand the input of this work, extract of VASP manual, only the part about tags I used, is given here. The complete guide of VASP can be found from their website:

http://cms.mpi.univie.ac.at/vasp/vasp/vasp.html

NEB calculation were performed with VTST tools, tags about NEB can be found here:

http://theory.cm.utexas.edu/vtsttools/neb.html

Tags list:

SYSTEM: a title string for user to identify.

IBRION: how the ions update and move. 2 is conjugate gradient algorithm; 3 is damped molecular dynamics; 5 is finite differences, used for determining the second derivatives, including Hessian matrix and phonon frequencies.

ISMEAR: how the partial occupancies are set for each orbital. 1 is method of Methfessel-Paxton order 1; -5 is tetrahedron method with Blöchl corrections.

ISIF: whether the stress tensor is calculated. 0 is that do not calculate stress tensor and cell change; 2 is that calculate stress tensor and do not change the cell.

ISPIN: whether spin polarized calculations are performed. 2 is turn on spin polarized calculation.

ISYM: symmetry switch. 0 is switching off symmetry.

ICHARG: how to construct initial charge density. 2 is taking superposition of atomic charge densities.

IOPT: which method is used for finding energy path and saddle point. 3 is Quick-Min.

PREC: precision. Accurate is a combine of many parameters.

ALGO: a convenient option to specify the electronic minimization algorithm. Fast is a robust mixture of Davidson and RMM-DIIS algorithm.

LORBIT: whether RWIGS line is required and DOSCAR & PROCAR files are written. FALSE is line required and files written, 11 is line not read and files written.

LREAL: whether the projection operators are evaluated in real-space or in reciprocal space. Auto is that projection done in real space, fully automatic optimization of projection operators.

LCHARG: whether the charge densities files are written. FALSE is not writing.

LWAVE: whether the orbitals file is written. FALSE is not writing.

LCLIMB: whether climbing image algorithm is turned on. FALSE is turning off.

ENCUT: cut-off energy for plane wave basis set.

EDIFF: defines the global break condition for the electronic selfconsistency-loop. The relaxation of the electronic degrees of freedom will be stopped if the total energy change and the band structure energy change between two steps are both smaller than this.

EDIFFG: defines the break condition for the ionic relaxation loop. If the change in the total energy is smaller than this value between two ionic steps relaxation will be stopped. If the value is negative, it means the relaxation will stop if all forces are smaller than this value.

SIGMA: the width of the smearing.

NEDOS: number of grid points in DOS.

POTIM: a scaling constant for the forces.

NFREE: how many displacements are used for each direction and ion.

NSW: the maximum number of ionic steps.

NELM: the maximum number of electronic selfconsistency steps.

NELMDL: the number of non-selfconsistent steps at the beginning. Negative value means the delay only applied for the start-configuration.

NPAR: the calculation is preformed parallelly. This is how many parts the total number cores are divided into.

ICHAIN: which method to run. 0 is NEB.

IMAGES: how many images between the fixed endpoints.

SPRING: the spring constant between the images. Negative value turns on nudging.

B. Optimization INCAR example

SYSTEM = opt

IBRION = 2
ISMEAR = 1
ISIF = 2
ISPIN = 2
ISYM = 0
ICHARG = 2

PREC = Accurate
ALGO = FAST
LORBIT = FALSE
LREAL = Auto
LCHARG = FALSE
LWAVE = FALSE

ENCUT = 520
EDIFF = 0.0001
EDIFFG = -0.02
SIGMA = 0.2

NSW = 500
NELM = 50
NELMDL = -5
NPAR = 4

C. Density of state calculation INCAR example

SYSTEM = DOS

IBRION = 2
ISMEAR = -5
ISIF = 2
ISPIN = 2
ISYM = 0
ICHARG = 2

PREC = Accurate
ALGO = FAST
LORBIT = 11
LREAL = Auto
LCHARG = FALSE
LWAVE = FALSE

ENCUT = 520
EDIFF = 0.00001
SIGMA = 0.2
NEDOS = 3000

NSW = 300
NELM = 100
NPAR = 4

D. Frequency calculation INCAR example

```
SYSTEM = FRE

IBRION  = 5                    ENCUT  = 520
ISMEAR = 1                     EDIFF   = 0.0001
ISIF       = 2                 SIGMA  = 0.2
ISPIN     = 2                  POTIM  = 0.002
ISYM      = 0                  NFREE  = 2
ICHARG = 2

                               NSW     = 1
PREC     = Accurate            NELM    = 50
LORBIT  = FALSE                        NELMDL= -5
LREAL   = Auto                 NPAR    = 4
LCHARG          = FALSE
LWAVE  = FALSE
```

E. Transition states calculation INCAR example

```
SYSTEM = NEB

IBRION  = 3                    ENCUT  = 520
ISMEAR = 1                     EDIFF   = 0.0001
ISIF       = 0                 EDIFFG = -0.05
ISPIN     = 2                  SIGMA  = 0.2
ISYM      = 0                  POTIM  = 0.0
ICHARG = 2
IOPT      = 3

                               NSW     = 1000
                               NELM    = 50
PREC     = Accurate            NELMDL= -5
LORBIT  = FALSE                        NPAR    = 4
LREAL   = Auto
LCHARG          = FALSE                ICHAIN  = 0
LWAVE  = FALSE                         IMAGES = 4
LCLIMB = FALSE                 SPRING  = -5
```